

1 **Assessing land-ocean connectivity via Submarine Groundwater Discharge**  
2 **(SGD) in the Ria Formosa Lagoon (Portugal): combining radon**  
3 **measurements and stable isotope hydrology**

4

5 C. Rocha\*<sup>1</sup>, C. Veiga-Pires<sup>1,2</sup>, J. Scholten<sup>3</sup>, K Knoeller<sup>4</sup>, D.R. Gröcke<sup>5</sup>, L. Carvalho<sup>1,2</sup>,  
6 J. Anibal<sup>1,2</sup> and J. Wilson<sup>1</sup>

7 <sup>1</sup>Biogeochemistry Research Group, Geography Department, School of Natural  
8 Sciences, Trinity College Dublin, Dublin 2, Ireland.

9 <sup>2</sup>CIMA-Marine and Environmental Research Center, Universidade do Algarve,  
10 Portugal

11 <sup>3</sup>Institute of Geosciences, University of Kiel, Germany

12 <sup>4</sup>UFZ - Helmholtz Centre for Environmental Research Leipzig/Halle, Germany

13 <sup>5</sup>Department of Earth Sciences, Durham University, South Road, Durham, County  
14 Durham, DH1 3LE, UK

15 \*Corresponding author. Email: [rochac@tcd.ie](mailto:rochac@tcd.ie)

16

17 **Abstract**

18 Natural radioactive tracer-based assessments of basin-scale Submarine  
19 Groundwater Discharge (SGD) are well developed. However, SGD takes place in  
20 different modes and the flow and discharge mechanisms involved occur over a  
21 wide range of spatial and temporal scales. Quantifying SGD while discriminating  
22 its source functions therefore remains a major challenge. Yet, correctly  
23 identifying both the fluid source and composition is critical. When multiple  
24 sources of the tracer of interest are present, failure to adequately discriminate  
25 between them leads to inaccurate attribution and the resulting uncertainties will  
26 affect the reliability of SGD solute loading estimates. This lack of reliability then  
27 extends to the closure of local biogeochemical budgets, confusing measures  
28 aiming to mitigate pollution.

29 Here, we report a multi-tracer study to identify the sources of SGD, distinguish  
30 its component parts and elucidate the mechanisms of their dispersion  
31 throughout the Ria Formosa — a seasonally hypersaline lagoon in Portugal. We  
32 combine radon budgets that determine the total SGD (meteoric + recirculated  
33 seawater) in the system with stable isotopes in water ( $\delta^2\text{H}$ ,  $\delta^{18}\text{O}$ ), to specifically  
34 identify SGD source functions and characterize active hydrological pathways in  
35 the catchment. Using this approach, SGD in the Ria Formosa could be separated  
36 into two modes, a net meteoric water input and another involving no net water  
37 transfer, i.e., originating in lagoon water re-circulated through permeable  
38 sediments. The former SGD mode is present occasionally on a multiannual  
39 timescale, while the latter is a dominant feature of the system. In the absence of  
40 meteoric SGD inputs, seawater recirculation through beach sediments occurs at a  
41 rate of  $\sim 1.4 \times 10^6 \text{ m}^3 \text{ day}^{-1}$ . This implies the entire tidal-averaged volume of the  
42 lagoon is filtered through local sandy sediments within 100 days ( $\sim 3.5$  times a  
43 year), driving an estimated nitrogen (N) load of  $\sim 350 \text{ Ton N y}^{-1}$  into the system  
44 as  $\text{NO}_3^-$ . Land-borne SGD could add a further  $\sim 61 \text{ Ton N y}^{-1}$  to the lagoon. The  
45 former source is autochthonous, continuous and responsible for a large fraction  
46 (59%) of the estimated total N inputs into the system via non-point sources,  
47 while the latter is an occasional allochthonous source capable of driving new  
48 production in the system.

## 49 **1. Introduction**

50 Freshwater inputs into the coastal zone are important pathways for the transfer  
51 of land-borne solutes and particulates into the sea. Even if channeled freshwater  
52 flows such as rivers are relatively well-gauged world wide, sub-surface sources  
53 are more difficult to quantify in coastal settings. This difficulty has hindered the  
54 understanding of current drivers of coastal ecosystem decline (Carpenter et al.  
55 1998; Finkl and Krupa 2003). Indeed, on a global scale, an estimated 6 % of the  
56 freshwater input into the sea, carrying an anticipated 52% of the total dissolved  
57 salts crossing the land-ocean interface, was estimated to occur via SGD-  
58 Submarine Groundwater Discharge by Zektser and Loaiciga (1993). This early  
59 estimate has since been updated by Kwon et al (2014), who show that global SGD  
60 is 3-4 times greater than the freshwater flow into the oceans by rivers. This  
61 revision means that SGD is by far the largest contributor of terrestrial solutes to  
62 the global ocean, hence implying that some global biogeochemical budgets of  
63 major elements need revision. Yet, mass flows defining the contribution of SGD  
64 to coastal biogeochemical budgets are difficult to quantify in a systematic way  
65 (Burnett et al. 2001a).

66 To understand the contribution of groundwater/seawater interactions to marine  
67 biogeochemistry (Moore 1996; Moore and Church 1996; Church 1996, Moore  
68 2006), the definition of SGD encompasses any flow of water across the sea floor,  
69 regardless of fluid composition or driving force (Burnett et al. 2003). This is  
70 because reactivity of solutes when meteoric and sea water mix and travel  
71 through porous media significantly alters the composition of the discharging  
72 water with respect to both original contributions (Moore 1999; Moore 2010).  
73 Submarine Groundwater Discharge is therefore not limited to fresh groundwater  
74 discharge but includes seawater recirculation through coastal sediments (Li et al.  
75 1999) and seasonal repositioning of the salt/freshwater interface (Michael et al.  
76 2005; Edmunds 2003; Santos et al. 2009). All of these promote changes to the  
77 rates of transfer, mixing and chemical reaction at the subterranean estuary  
78 (Moore 1999; Charette et al. 2005; Charette and Sholkovitz 2006; Robinson, et al.  
79 2007) altering the original chemical signatures in a non-uniform way at system  
80 scale (Slomp and van Cappellen 2004; Spiteri et al. 2008).

81 Tracer-based assessments of basin-scale SGD are well developed (Burnett et al.  
82 2001a,b; Burnett et al. 2003; Burnett et al. 2008), but because the flow and  
83 discharge mechanisms involved cover a wide range of spatial and temporal  
84 scales (Bratton 2010; Santos et al. 2012), quantifying SGD while discriminating  
85 its source functions is still a challenge (e.g., Mulligan and Charette 2006). Indeed,  
86 the most common approaches to estimate SGD are: a) radioactive tracer studies  
87 specifically looking at radon ( $^{222}\text{Rn}$ ,  $T_{1/2} = 3.8$  days) (Burnett et al. 2001a,b) and  
88 radium isotopes (Moore and Arnold 1996); b) direct measurement of discharge  
89 fluxes over small areas (Lee 1977, Michael et al 2003, Taniguchi et al 2003); and  
90 c) modeling. Direct measurements offer limited spatial coverage and are labor  
91 intensive (e.g., Leote et al. 2008), making reliable flux estimates at the system  
92 scale difficult. Modeling approaches depend on the water and/or salt budgets,  
93 hydrograph separation techniques, or descriptions of interfacial flow dynamics  
94 based on Darcy's law. Frequently, however, they incorporate assumptions of a  
95 steady state inventory and homogeneity of hydraulic conductivity over large  
96 scale-lengths and fail to include seawater recirculation. In addition, there is often  
97 a mismatch between spatial and/or temporal scale of the model outputs and  
98 those necessary to close coastal biogeochemical budgets (Prieto and Destouni  
99 2010).

100 Radioactive tracer studies produce spatially integrated estimates of flux (Cable et  
101 al. 1996; Moore 1996), while simultaneously dampening the effects of short-term  
102 variability (Burnett et al. 2001a). However, while radon budgets produce an  
103 estimate of 'total' SGD, i.e., freshwater inputs + re-circulated seawater (Mulligan  
104 and Charette 2006), radium budgets primarily assess the salty component of SGD  
105 given that radium is normally absent in fresh groundwater but might be  
106 mobilized from sediment particles in case of saline water influence (Webster et  
107 al. 1995). Even so, the variety of ubiquitous temporally and spatially variable  
108 sediment-water exchange mechanisms that also act as sources of radon (Cable et  
109 al. 2004; Martin et al. 2004; Colbert, et al. 2008a,b) and short-lived radium  
110 isotopes to surface waters (Webster et al. 1994; Hancock and Murray 1996;  
111 Hancock et al. 2000; Colbert and Hammond 2007; Colbert and Hammond 2008;  
112 Gonnee et al. 2008) cannot be ignored. Correctly identifying both the fluid

113 source and composition is thus an important task (Mulligan and Charette 2006;  
114 Burnett et al. 2006). When multiple tracer sources of interest are present, failure  
115 to adequately discriminate between them will lead to inaccurate attribution and  
116 the resulting uncertainties will affect the reliability of SGD solute loading  
117 estimates.

118 Indeed, as noted by Beck et al. (2007), SGD-borne chemical load into coastal  
119 systems is usually predicted by combining measurements of source composition  
120 with SGD estimates. Linking these two datasets requires care and is underpinned  
121 by our ability to correctly identify and quantify the different SGD pathways into  
122 any one system. This is because the final SGD solute-load estimate not only  
123 depends on how accurate our recognition of the SGD source functions is, but also  
124 on the ability to track their path within the system, since this is required to  
125 evaluate the biogeochemical history of the source components prior to their  
126 mixture into receiving waters. Not fulfilling this requisite therefore constitutes  
127 the major obstacle to prognosticate upper boundary or 'potential' SGD-related  
128 impact, and more importantly, confidently attribute causality. Indeed, the  
129 endmember is usually the greatest source of uncertainty in any tracer or solute  
130 mass balance. It follows that determining the endmember concentration in the  
131 area(s) most likely to be the source(s) of groundwater would decrease  
132 uncertainty in SGD estimates, on the one hand, and in biogeochemical budgets  
133 derived from those estimates on the other. The current panorama of SGD  
134 research at the system scale therefore begs the question of which end-member to  
135 use when selecting a source solute concentration in attempts to quantify  
136 pollutant fluxes associated with SGD.

137 We contribute an answer to this conundrum with a study conducted in a  
138 seasonally hypersaline lagoon in southern Portugal where we combine two  
139 datasets: radon surveys are used to determine total SGD in the system while  
140 stable isotopes in water ( $^2\text{H}$ ,  $^{18}\text{O}$ ) are used to specifically identify SGD sources  
141 and characterize active hydrological pathways. We show that, in combination  
142 with radon budgeting, stable isotope hydrology is a reliable tool to identify  
143 different SGD sources in a very complex coastal system, even though it hasn't  
144 been used to this end before. This underuse of the methodology has two main

145 reasons. The first is a disciplinary divide: the technique has been the domain of  
146 freshwater hydrologists; correlations between  $\delta^{18}\text{O}$  and  $\delta^2\text{H}$  are central to  
147 research into the effect of evaporation and mixing on surface waters (Gat et al.  
148 1994, Gibson and Edwards 2002) and contribute to the disentanglement of  
149 different water sources affecting catchments (Rodgers et al. 2005). The other is  
150 the paucity of paired  $\delta^{18}\text{O} - \delta^2\text{H}$  data on coastal seawater (e.g., Rohling 2007),  
151 even if stable isotope datasets might help constrain the origins of freshwater  
152 inputs into the ocean when coupled with salinity data (Munksgaard et al. 2012,  
153 Schubert et al 2015), or as part of a methodological arsenal in SGD studies  
154 combining physical and chemical measurements with radioactive and stable  
155 isotope tracers (e.g., Povinec et al 2008). Hence we also bridge the disciplinary  
156 gap between marine chemists and hydrogeologists currently extant in SGD  
157 studies by using a combined approach merging techniques from both disciplines.

158 The occurrence of SGD comprising significant freshwater contributions was first  
159 detected in the Ria Formosa in 2006–2007 and subsequently described as a  
160 prominent source of nutrients, in particular nitrogen derived from fertilizers, to  
161 the lagoon (Leote et al. 2008; Rocha et al. 2009; Ibánhez et al. 2011, 2013).  
162 However, the unpredictable nature of freshwater availability in the region,  
163 coupled with a mixed-source (i.e., a variable mix of groundwater abstraction and  
164 surface water collected in reservoirs) management of public water supply to  
165 meet demand (Monteiro and Costa Manuel 2004; Stigter and Monteiro 2008),  
166 made it unclear whether meteoric groundwater would be a persistent feature of  
167 SGD in the system. This made it difficult to clarify the contribution of SGD to the  
168 nitrogen budget of the Ria Formosa, with obvious consequences to  
169 environmental management strategies. The overarching aims of the study were  
170 therefore to identify the sources of SGD, distinguish its component parts and  
171 elucidate the mechanisms of their dispersion throughout the Ria Formosa. The  
172 outcomes are then employed to distinguish and quantify nitrogen loads carried  
173 into the lagoon by different SGD modes.

174

175

## 176 2. Study Site

177

### 178 2.1. Geomorphology and Hydrodynamics

179 Located in South Portugal (36°58'N, 8°02'W – 37°03'N, 7°32'W), the Ria Formosa  
180 (Fig. 1) is a leaky (Kjerfve 1986) lagoon system separated from the Atlantic by a  
181 multi-inlet barrier island cordon. The system covers a surface area of ~111 km<sup>2</sup>  
182 and has an average depth of 2 m. The tide is semi-diurnal with average ranges of  
183 2.8 m for spring tides and 1.3 m for neap tides (Vila-Concejo et al. 2004; Pacheco  
184 et al. 2010a). The maximum average tidal volume as estimated by the Navy  
185 Hydrographical Institute (IH 1986) is ~140×10<sup>6</sup> m<sup>3</sup>. Lagoon water is exchanged  
186 with the Atlantic Ocean through six tidal inlets with an average tidal flux of  
187 ~8×10<sup>6</sup> m<sup>3</sup> (Balouin et al. 2001). Estimates for the submerged area amount to  
188 ~55km<sup>2</sup> at high spring tide and between 14 and 22 km<sup>2</sup> at low spring tide (IH,  
189 1986). From west to east (Fig. 1), inlets (*Barra*, in Portuguese) are identified as  
190 Ancão, Faro-Olhão (*Barra Nova*), Armona (*Barra Velha*), and Fuzeta, Tavira and  
191 Lacem. Barra Nova, Barra Velha and Ancão jointly capture ~90% of the total tidal  
192 prism: 61%, 23% and 8% of the total flow during spring tides and 45%, 40% and  
193 ~5% during neap tides, respectively (Pacheco et al. 2010). With the exception of  
194 the Barra Nova all inlets are ebb dominated with residual circulation directed  
195 seaward (Dias and Sousa 2009).

196

### 197 2.2. Hydrogeological setting

198 The regional climate is semi-arid, with average annual temperature of 17 °C and  
199 averages of 11°C and 24°C during winter and summer. The surrounding  
200 watershed covers 740 km<sup>2</sup> and receives effective precipitation of 152 mm/year  
201 (Salles 2001), corresponding to an annual rainfall amount of ~1.2×10<sup>6</sup> m<sup>3</sup>. There  
202 are five minor rivers and fourteen streams discharging into the lagoon. Most are  
203 ephemeral and dry out during the summer, the exception being the River Gilão,  
204 which intermittently discharges almost directly into the Atlantic through the  
205 Tavira inlet at the eastern limits of the system.

206 Three aquifer systems (Fig. 1) border the Ria Formosa (Almeida et al. 2000).  
207 These are the Campina de Faro (M12), Chão de Cevada – Quinta João de Ourém  
208 (M11) and São João da Venda – Quelfes (M10). The main lithologies supporting  
209 these units are Plio-Quaternary, Miocene and Cretaceous formations, comprising  
210 respectively Pliocene sands and gravels, Quaternary dunes and alluvial deposits;  
211 sandy limestones of marine facies; and limestones and detritic limestones. The  
212 oldest formation dips to the south, and is found at depths in excess of 200 m near  
213 the city of Faro. It is overlain by the Miocene formation extending below the Ria  
214 Formosa into the Atlantic Ocean. Sand dunes, sands and gravels of the Plio-  
215 Quaternary cover the Miocene and Cretaceous formations within the coastal  
216 area. The Campina de Faro (M12, Fig. 1, 86.4 km<sup>2</sup>) comprises a superficial  
217 unconfined aquifer (Pleistocene deposits) with a maximum thickness of 30 m  
218 and an underlying Miocene confined multi-layered aquifer, which Engelen and  
219 van Beers (1986) suggest discharges directly into the Atlantic Ocean bypassing  
220 the lagoon. The unconfined Pleistocene aquifer is hydraulically connected to the  
221 underlying Miocene aquifer. The São João da Venda-Quelfes aquifer (M10, Fig. 1,  
222 113 km<sup>2</sup>) includes a surface 75 m thick layer of Wealdian facies and an  
223 underlying Cretaceous layer of loamy limestone. It contacts with the M12  
224 (Campina de Faro) aquifer and the M11 (Chão de Cevada-Quinta João de Ourém)  
225 to the south, and the main flow direction on the eastern side is towards the  
226 southeast. Groundwater flow is divergent toward the southeast and the  
227 southwest from a central point (Almeida et al. 2000).

228 In the 1980's nitrate contamination from inorganic fertilizers was detected in  
229 both Quaternary and Miocene sub-units of the Campina de Faro (M12) aquifer  
230 (Almeida and Silva 1987). Average concentrations were 8.3 mmol L<sup>-1</sup> with some  
231 samples containing in excess of 28.6 mmol L<sup>-1</sup>. More recently, Lobo-Ferreira et al  
232 (2007) calculated an average concentration of 2.1 mmol L<sup>-1</sup> over the entire  
233 aquifer, an estimate that is consistent with the long-term (1995–2011) average  
234 ( $n=31$ ) of  $1.87 \pm 0.35$  mmol L<sup>-1</sup> nitrate concentration reported from public  
235 groundwater quality data (<http://www.snirh.pt>) in a monitoring borehole in  
236 Montenegro, close to the boundary with the Ria. During 2006–2007, nitrate and  
237 ammonium concentrations of up to 187 and 40  $\mu\text{mol L}^{-1}$  respectively were



238 measured in SGD collected by seepage meters deployed at the littoral zone of the  
239 barrier islands. The upper bound mean nitrate concentration in the freshwater  
240 component of SGD was estimated at  $\sim 0.4 \text{ mmol L}^{-1}$  (Leote et al. 2008).

241

### 242 **3. Methods**

#### 243 **3.1. Radon measurements**

##### 244 **3.1.1. Lagoon radon inventory during ebb and flood**

245 Water radon ( $^{222}\text{Rn}$ ) content was measured continuously in-situ using two  
246 electronic Durrige RAD-7 radon-in-air monitors deployed in tandem on a  
247 moving rubber boat during winter (December 2009) and spring (May 2010).  
248 Each monitor was coupled to an air-water equilibrator (Durrige RAD-Aqua  
249 Accessory) via its own air loop. Non-cavitating centrifugal pumps were used to  
250 flush water from  $\sim 50 \text{ cm}$  below the water surface directly into the equilibrators,  
251 at a flow rate of  $1.8\text{--}2.5 \text{ L min}^{-1}$ . HOBO<sup>™</sup> temperature sensors and a CTD diver  
252 (Schlumberger<sup>™</sup>) continuously recorded the temperature in the mixing  
253 chambers and the salinity and temperature of the water being pumped. Counting  
254 interval was set at 20 minutes on each RAD-7 monitor, with the two machines  
255 staggered by a 10-minute period, allowing for simultaneous replication of 20-  
256 minute integration periods over the route and increased temporal resolution.  
257 Full equilibration between the air within the air-loop and the pumped seawater  
258 was achieved before surveys started. Sampling began near low tide and  
259 continued without interval for 24 hours. The survey path, recorded with an on-  
260 board GPS unit, and the timing were designed to cover the main navigable  
261 sectors of the whole lagoon at different tidal stages (ebb and flood) within the  
262 course of two complete tidal cycles. In-water radon activity was calculated from  
263 the temperature and salinity dependant gas/water equilibrium (Schubert et al.  
264 2012). Radon activities obtained this way were then corrected by the local  $^{226}\text{Ra}$   
265 supported activity, to obtain excess (i.e., unsupported) radon activities. For mass  
266 balance purposes, the excess radon inventories were calculated by multiplying  
267 the unsupported radon activity from the continuous measurements by the local

268 bathymetric depth, and then normalized to mean tidal height (Burnett and  
269 Dulaiova 2003).

270

### 271 **3.1.2. Tidal variability of Radon activity at fixed locations**

272 Time series of radon activity were obtained synchronously at two fixed locations  
273 within the Faro channel (Fig. 1), during June 2010. The locations were chosen in  
274 order to gain insight into the exchange of radon between the lagoon and the  
275 adjacent coastal zone through the Barra Nova (Fig. 1) and between the inner  
276 reaches of the lagoon and the latter via the Faro channel (Quatro Águas, Fig. 1).  
277 Radon activity was measured as described previously, with the added  
278 deployment of a CTD diver (Schlumberger™) recording depth, salinity and  
279 temperature at the bottom of the channel. The Barra Nova tidal cycle data was  
280 then used to calculate the net exchange of radon with the adjacent coastal zone  
281 through the main inlet, assuming a vertically well-mixed water column. Exchange  
282 of radon through the inlet cross section driven by oscillating tidal flow was  
283 determined by first calculating the instantaneous directional flux,  $F_{Rn}(\Delta t)$ , where  
284  $\Delta t$  is the counting interval,  $ARn(\Delta t)$  the activity of radon integrated across the  
285 counting interval and  $dh/dt$  the change in tidal height (r.m.s.l.) occurring over  
286 that interval:

$$287 \quad F_{Rn}(\Delta t) = \left( \frac{dh}{dt} \right) \times ARn(\Delta t) \quad (1)$$

288 The total radon flux was obtained for both the flood and ebb periods by  
289 integrating the instantaneous directional fluxes calculated for each counting  
290 period (Eq. 1) over time. Radon outflow (when fluxes were negative) and inflow  
291 (when positive) are hence obtained for each complete semi-tidal period.  
292 Difference between successive outflow and inflow periods gives us the net  
293 transfer across the channel during a complete tidal cycle. Data for a minimum of  
294 three successive complete tidal cycles, giving three different values for net  
295 transfer, were used, and the exchange values determined for each cycle were  
296 then averaged to obtain the net exchange flux along the channel at each sampling  
297 site.

### 298 **3.1.3. Complementary radon measurements**

299 Measurements of air temperature, wind speed and atmospheric radon activities  
300 were taken on land, while the lagoon radon survey progressed. Atmospheric  
301 evasion losses (radon degassing flux) were calculated as described in Burnett  
302 and Dulaiova (2003), using the equations given in Macintyre et al. (1995) and  
303 Turner et al. (1996). Sediment-water diffusive fluxes of radon were measured as  
304 described in Corbett et al. (1998) in samples ( $n=16$ ) collected throughout the  
305 lagoon and directly analyzed in the laboratory upon collection. To obtain these  
306 samples, undisturbed sediment cores (35 cm length) were collected using  
307 polycarbonate core-liners ( $\varnothing$  5.5 cm) in both sub-tidal ( $n=8$ ) and intertidal  
308 environments ( $n=8$ ), with each environment sub-sampled for sandy and muddy  
309 sediments in equal proportions. Resulting fluxes from all analyzed cores were  
310 then averaged and the latter value, with its associated uncertainty, used in  
311 subsequent mass balance calculations.

### 312 **3.1.4. SGD flux estimates based on Rn mass balances**

#### 313 **Lagoon Radon budget under steady state assumptions**

314 The advective flux of radon associated with SGD is determined by the closure of a  
315 radon budget incorporating all known sources and sinks of radon in the system  
316 (Burnett and Dulaiova 2003). Mass conservation accounting for the change in  
317 inventory of radon was expressed as:

$$318 \left( \frac{dI_{Rn}}{dt} \right) = Rn_{diff} - Rn_{dg} - Rn_{dy} + (Rn_{imp} - Rn_{exp}) + Rn_{adv} \quad (2)$$

319 where  $I_{Rn}$  is the radon inventory measured within the Ria Formosa,  $t$  the time,  
320  $Rn_{diff}$  the Radon flux across the sediment water interface by diffusion,  $Rn_{dg}$  the  
321 radon degassing flux, i.e., atmospheric evasion,  $Rn_{dy}$  the radon decay flux in the  
322 lagoon (i.e., the internal sink),  $Rn_{exp}$  and  $Rn_{imp}$  the exchange fluxes across inlets,  
323 seaward (export) and landward (import), respectively, and  $Rn_{adv}$  the advective  
324 Radon flux putatively associated with SGD. Usually, an additional term  
325 accounting for the radon influx via river flow is added if the water and  
326 particulate flux associated with river discharge is significant. However, the only  
327 perennial river in the Ria Formosa is the Gilão, located in the eastern limit of the

328 lagoon. Salinity measured at the estuary mouth was 29.6 (Table S1), which in  
 329 combination with its location implied very low if any inputs of freshwater  
 330 carrying radon into the system so we neglected the term.

331 Assuming steady state of all sinks and sources over the lifetime of radon in the  
 332 system, then:

$$333 \quad \left( \frac{dI_{Rn}}{dt} \right) = 0, (Rn_{imp} - Rn_{exp}) = Rn_{net} \Rightarrow Rn_{adv} = Rn_{diff} - Rn_{dg} - Rn_{dy} + Rn_{net} \quad (3)$$

334 where  $Rn_{net}$  is the residual Radon exchange flux with the ocean.

335

### 336 **Mass balance of radon during ebb and flood**

337 Inventories of radon in the lagoon were determined during ebb and flood. Taking  
 338 the tide as a travelling wave, the change in inventory of radon as the tide floods  
 339 and ebbs has to be balanced by all known radon fluxes occurring within the  
 340 traversed system during the travel period. If we then take the mean tide level  
 341 (MTL) as a reference, it follows that the  $Rn_{adv}$  term may be calculated for  
 342 different periods: the period ( $T$ ) at which the tidal height in the lagoon is below  
 343 MTL ( $Rn_{adv}(T < MTL)$ ), i.e., the trough of the tidal wave or low tide, and the one  
 344 when it is above MTL ( $Rn_{adv}(T > MTL)$ ), corresponding to the peak of the wave, or  
 345 high tide. Assuming constant mean amplitude for the tidal wave the  
 346 corresponding mass conservation equations may be written as follows:

$$347 \quad Rn_{adv}(T < MTL) = \frac{If - Ie}{\Delta t} - (R_{diff} - Rn_{dg} - Rn_{dy} + Rn_{net}) \quad (4a)$$

$$348 \quad Rn_{adv}(T > MTL) = \frac{Ie - If}{\Delta t} - (R_{diff} - Rn_{dg} - Rn_{dy} + Rn_{net}) \quad (4b)$$

349 where  $If$  and  $Ie$  are the flood and ebb inventories of radon in the lagoon,  $\Delta t$  the  
 350 period of the wave ( $\sim 0.5$  day) and  $Rn_{adv}(T < MTL)$  and  $Rn_{adv}(T > MTL)$  the radon  
 351 advective fluxes associated with each semi-period (trough and peak stages,  
 352 respectively). The corresponding continuity equation, describing the net  
 353 advective flux of radon on a daily basis (note that for semi-diurnal tidal  
 354 periodicity we assume 1 day  $\sim 2$  tidal periods), is then:

355 
$$\frac{Rn_{adv}}{2\Delta t} = \frac{Rn_{adv}(T < MTL)}{2} + \frac{Rn_{adv}(T > MTL)}{2} \quad (4c)$$

356

## 357 **3.2. Stable isotope hydrology**

### 358 **Sampling location and timing**

359 Water samples for stable isotope analysis were collected in triplicate from all  
360 possible water sources to the lagoon (end-members) during winter on various  
361 occasions between 2007 and 2011 (Table 2 and S1). These include: the marine  
362 end-member, sampled in 2009; groundwater from local aquifer units (M10, M12,  
363 unconfined aquifer lenses in the Barrier island) taken from boreholes and wells  
364 (Fig. 1), in January 2007 and December 2009 and 2010; precipitation, taken at  
365 the city of Faro in December 2009; beach porewater collected in January 2007,  
366 December 2010 and January 2011. In 2007, samples were extracted from 50 cm  
367 below the sediment-water interface at various locations along the Ancão  
368 peninsula's inner dune cordon (Fig 1), while in 2010 and 2011 they originated  
369 from various depths in the sediment (2 to 7 m below r.m.s.l.) and were collected  
370 using a cross-shore array of nested, multi-level sampling piezometers (Fig 1)  
371 installed in the inner margin of the outer dune cordon in January 2010 at the  
372 point of maximal freshwater seepage rates found in 2007. Surface water  
373 reservoirs near Quinta do Lago used for irrigation and settling lagoons in the  
374 wastewater treatment plant near the city of Faro (WWTP) were sampled in July  
375 2007, the river Gilão (Fig 1), in December 2010, and surface water from the  
376 lagoon was sampled during flood tide (western sector, Fig 1) in January 2007  
377 and during both high and low tide in December 2009.

378 For the latter, quasi-synoptic distributions of  $\delta^{18}\text{O}$  and  $\delta^2\text{H}$  in water at different  
379 tidal stages were obtained. For this purpose, we followed the division of the  
380 lagoon into two sectors, comprising western and eastern areas (see Fig. 1), with  
381 the separation line lying between the city of Faro and the Barra Nova. This  
382 division was based on the known divergent flow of groundwater in the M12 and  
383 M10 aquifers from a central point (Rio Seco – Chelote line, Fig 1) as described  
384 (see Section 2.2) in Almeida (2000). High-powered boats were deployed, one

385 from the city of Faro, on the 2<sup>nd</sup> December 2009 and the other from the city of  
386 Olhão, on the 5<sup>th</sup> December 2009 (Fig 1). The boats followed the tide outflow (or  
387 inflow) while covering all the pre-defined sampling points (western sector  
388 stations 1-5 and 1B to 5B, eastern stations A to I, Fig. 1). Each region of the  
389 lagoon was covered at each tidal stage in no more than two hours around slack  
390 tide. Coastal seawater adjacent to the Ria Formosa was sampled two nautical  
391 miles (~3.8 km) offshore from the town of Quarteira to the west and from the  
392 Barra Velha (Armona inlet, Fig. 1, reference J).

### 393 **Sampling and analytic methodology**

394 Water was directly filtered through Rhizon SMS™ membranes into sterile glass  
395 Vacutainer™ vials in the field. Subsequently, the cap area including the rubber  
396 septum was sealed with a layer of hot glue encased in Parafilm™. The vials were  
397 kept preserved at 4°C until analysis could occur (typically within six months  
398 from the date of collection). Samples were sent for standard analysis of  $\delta^{18}\text{O}$  and  
399  $\delta^2\text{H}$  to GEOTOP Canada (Micromass Isoprime™ dual inlet coupled to an  
400 Aquaprep™ system), Durham University (LGR - liquid water isotope analyser,  
401 DT100) and at UFZ's stable isotope laboratory facilities in Halle, Germany (Laser  
402 cavity ring-down spectroscopy (Laser CRDS) Picarro water isotope analyzer L-  
403 1120i). Following standard reporting procedures (Craig 1961a), delta values ( $\delta$ )  
404 are reported as deviations in permil (‰) from the Vienna Standard Mean Ocean  
405 Water (V-SMOW), such that  $\delta_{\text{sample}} = 1000((R_{\text{sample}}/R_{\text{V-SMOW}})-1)$ , where R is the  
406 relevant isotopic ratio (i.e., either  $^2\text{H}/^1\text{H}$  or  $^{18}\text{O}/^{16}\text{O}$ ). The mean analytical  
407 uncertainty is reported for each data point as  $\pm 1$  standard deviation (s.d.) of the  
408 mean of  $n$  analysis results obtained for  $n$  replicate samples in ‰ for  $\delta^{18}\text{O}$  and for  
409  $\delta^2\text{H}$  (see Table 2). Each laboratory uses stringent protocols and reporting of  
410 stable isotope values using internationally calibrated standards; hence, reported  
411 stable isotopes values of water between the different labs used in this study are  
412 directly comparable.

### 413 **Inter-annual comparability of isotopic data**

414 Sampling campaigns were carried out strategically following a field-adaptive  
415 protocol. Of primary concern was to capture the extent of temporal end-member

416 variability in isotopic signature under maximum freshwater flow (hi-flow)  
417 conditions, in order to a) guarantee coherence of source compositions to feed  
418 into mixing models when necessary while assessing the hydrology of the lagoon  
419 over wider temporal scales and b) minimizing logistics and costs while  
420 guaranteeing inter-comparability. For this purpose, winter season was chosen  
421 given that ~61% of the mean annual precipitation falls on the region between  
422 November and February (34% in the months of December and January). Stable  
423 isotope sampling in winter had the added advantage of minimizing kinetic effects  
424 over stable isotope signatures given the lower evaporation potential. Sampling in  
425 winter 2007 was exploratory, with two main objectives: firstly, to characterize  
426 isotopic signature of M12 groundwater and surface lagoon waters in the western  
427 sector, particularly in the area that could be potentially influenced by both SGD  
428 and the WWTP outflow under maximum dilution potential (hence high tide), and  
429 secondly, conduct an exploratory survey of potential seepage areas along the  
430 Ancão peninsula, keeping in mind that the location of at least one of the  
431 important SGD seepage sites was known (Leote et al, 2008). Detection of the  
432 isotopic signature of groundwater in porewaters at the seepage face at stations  
433 Pw\_e and Pw\_f (Table S1) led to the installation at their location of a nested  
434 piezometer transect array in January 2010. This was subsequently used to obtain  
435 porewater samples in the 2010/11 winter season (December 2010 and January  
436 2011).

437 To capture inter-annual variability, the M12 aquifer was sampled twice (winters  
438 of 2007 and 2009), with the provision of one common location (Ramalhete) for  
439 cross-referencing. Following the same reasoning, the M10 aquifer was sampled  
440 in December 2010 while simultaneously sampling Rio Seco (belonging to M12,  
441 Table S1). This ensured inter-comparability between groundwater isotopic  
442 signatures in 2009 and 2010. Campaigns were planned in advance considering  
443 the precipitation over the region to ensure similarity in the hydrological regime  
444 and ultimately guaranteeing inter-comparability of results. The sampling itself  
445 took place in dry conditions as much as possible, and never after intensive rain  
446 that could have promoted flooding (Table 2, Fig 4d). For example, while January  
447 2007 was a dry month (8.8 mm) compared to the historical average (138 mm),

448 the accumulated precipitation during the previous 3 months was 369.7 mm,  
449 consistent with the historical average (Table 2). By contrast, both December  
450 2009 and 2010 were relatively wet months (392.2 and 269.6 mm), but followed  
451 relatively dry 3-month periods (Table 2). So porewater samples were also taken  
452 in January 2011, hence complementing winter 2010/2011. January 2011  
453 followed a wet three-month period (414.7 mm) and was hence comparable with  
454 January 2007, also relatively dry but on the back of three wet months (369.7 mm  
455 cumulative). The combined dataset therefore contains results from repeated  
456 measurements for end-member isotopic composition under hi-flow conditions,  
457 across different years. These are in addition compared to historical data (table  
458 S1, Figure 4), leading to a temporally coherent quantitative overview of stable  
459 isotopic hydrology over the catchment.

460

## 461 **4. Results**

462

### 463 **4.1. Radon**

#### 464 **4.1.1. Spatial and temporal distribution**

465 The activity ranges and spatial distribution of  $^{222}\text{Rn}$  were similar in winter and  
466 spring. Because the weather was stormy during winter sampling, the  
467 uncertainties associated with determination of the radon evasion fluxes affecting  
468 the overall lagoon radon inventory were much higher than in spring (see Table  
469 1). Indeed, using a mass-balance used estimate fluxes has been shown sensitive  
470 to parameterization of gas exchange ( $k$ ) with the atmosphere, with potential  
471 uncertainties reaching 58% (Gilfedder et al, 2015). Hence only the spring survey  
472 data is presented and discussed. Excess radon activities measured in water  
473 varied between 3.5 and 37  $\text{Bq m}^{-3}$ , with a narrower range (5-25  $\text{Bq m}^{-3}$ )  
474 measured during ebb. The highest activities within the western sector during  
475 this stage ( $>25 \text{ Bq m}^{-3}$ ) were measured close to the city of Faro and in the  
476 Ramalhete channel, and close to the city of Olhão ( $\sim 20 \text{ Bq m}^{-3}$ ) in the eastern  
477 sector. Radon activities generally declined from the northwest to the southeast  
478 during ebb tide, with the lowest values ( $\sim 5 \text{ Bq m}^{-3}$ ) found in the Olhão channel



479 northeast of the Barra Nova. Conversely, the lowest activities during flood ( $\sim 5$   
480  $\text{Bq m}^{-3}$ ) were measured close to the Ancão inlet and at the outer end of the Faro  
481 channel, suggesting radon-poor coastal water intrusion during flood tide. The  
482 mean radon activities throughout the lagoon were  $19.3 \pm 4.74$  and  $15.59 \pm 4.54$   
483  $\text{Bq m}^{-3}$  respectively during flood and ebb. Relative accumulation of radon  
484 occurred at specific locations in the lagoon (Fig. 2a,b). The highest local water  
485 column inventories ( $318$  and  $267 \text{ Bq m}^{-2}$  during flood and ebb, respectively)  
486 were found in the Faro channel, covering stations 3 to A during ebb and 4 and 5  
487 during flood. The eastern sector water column inventories were much higher  
488 during flood than during ebb. Given the non-random spatial distribution of  
489 radon, the median of each dataset was used to calculate whole-lagoon  
490 inventories. The MAD (median absolute deviation, Hampel 1974) was then used  
491 to propagate uncertainty in the radon budget calculations (Table 1). Radon  
492 inventories (median  $\pm$  MAD) were  $54.2 \pm 17.8$  and  $74.0 \pm 17.6 \text{ Bq m}^{-2}$   
493 respectively during ebb and flood (Table 1).

494

#### 495 **4.1.2. Along-channel tidal radon fluxes**

496 Radon activity at Quatro Águas and Barra Nova was strongly anti-correlated with  
497 water level. At Quatro Águas, radon activities varied between 0 and  $40 \text{ Bq m}^{-3}$   
498 while at Barra Nova they varied between 1 and  $31 \text{ Bq m}^{-3}$ . Tidal variability at  
499 these two points was therefore consistent with the ranges in radon activities  
500 found during the lagoon survey. Time series of instantaneous Rn fluxes obtained  
501 as described by Eq. 1 are depicted for both locations in Fig. 3. The plots show  
502 consistency in the magnitude of upstream and downstream radon fluxes (grey  
503 area under the curves) through successive tidal cycles. The net daily tidal  
504 exchanges of radon through the Barra Nova and the Quatro Águas site ( $8.0 \pm 0.5$   
505  $\times 10^4$  and  $9.9 \pm 2.0 \times 10^3 \text{ Bq d}^{-1}$ , respectively) were both directed landward. This  
506 finding is consistent with the Barra Nova being a flood-dominated inlet  
507 (channeling  $\sim 64\%$  of the flood and  $\sim 59\%$  of the ebb prism of the Ria Formosa  
508 during spring tides: Dias and Sousa 2009; Pacheco et al. 2010b). To calculate the  
509 total residual exchange of radon between the Ria Formosa and the adjacent  
510 coastal area, we assumed the radon flux occurring at the other inlets to be

511 proportional in equal measure to the individual residual tidal prisms. After  
512 adjustment to the lagoon surface area at MTL the net exchange was just  $-9.3 (\pm$   
513  $1.6) \times 10^{-4} \text{ Bq m}^{-2} \text{ d}^{-1}$  (Table 1), so small as to be well within the uncertainty of all  
514 other quantities in the mass balance, implying that the radon inventory within  
515 the lagoon is controlled by internal fluxes.

516

#### 517 **4.1.3. SGD estimates based on radon mass balance**

518 Solving eq. 3 for a radon inventory of  $65.9 \pm 19.6 \text{ Bq m}^{-2}$  (Table 1) gave a result  
519 for  $R_{n\text{adv}}$  of  $7.14 \pm 5.18 \text{ Bq m}^{-2} \text{ day}^{-1}$ , which adjusted to the submerged area at  
520 mean tide level (Tett et al. 2003) gives an SGD derived radon flux of  $4.14 (\pm 3.00)$   
521  $\times 10^8 \text{ Bq day}^{-1}$  for the entire lagoon. Alternatively, the advective radon fluxes  
522 calculated as per equations 4a and 4b for low and high tide periods were  
523 respectively  $46.8 \pm 38.8$  and  $-32.5 \pm 27 \text{ Bq m}^{-2} \text{ day}^{-1}$ . The positive and negative  
524 signs imply an advective flux of radon ( $R_{n\text{adv}}$ ) into the lagoon water column at  
525 low tide, while a net loss occurs during high tide. The resultant net  $R_{n\text{adv}}$  (Eq. 4c)  
526 occurring during a full tidal period is  $7.15 \pm 8.4 \text{ Bq m}^{-2} \text{ day}^{-1}$ , statistically  
527 equivalent to the flux calculated via the assumption of steady state of the system  
528 over the lifetime of radon on a daily timescale (Eq 3), and yielding an equivalent  
529 SGD-derived radon flux of  $4.14 (\pm 4.87) \times 10^8 \text{ Bq day}^{-1}$  for the entire lagoon.

530

## 531 **4.2. Stable Isotope hydrology**

### 532 **4.2.1. $\delta^{18}\text{O}$ versus $\delta^2\text{H}$ relationships in the catchment**

533 Water stable isotope compositions obtained during this study, as well as Global  
534 Network of Isotopes in Precipitation (GNIP) (IAEA/WMO 2013) and other  
535 literature-sourced data (Carreira 1991) are listed in Table S1. During the 2007  
536 and 2009 winter surveys only unit M12 was sampled for fresh groundwater, but  
537 both the M12 and M10 aquifer units were sampled in winter 2010. Nonetheless  
538 the compositional range of fresh groundwater samples was quite similar: the  
539 most depleted values reported had a  $\delta^{18}\text{O}$  value of  $-5.09 \text{ ‰}$  (Pechão Gimno, M10)  
540 and a  $\delta^2\text{H}$  value of  $-27.79 \text{ ‰}$  (Gambelas, M12) while the most enriched had a  
541  $\delta^{18}\text{O}$  value of  $-3.46 \text{ ‰}$  (Rio Seco, M12) and a  $\delta^2\text{H}$  value of  $-21.45 \text{ ‰}$  (Zona

542 industrial, M12). The compositional ranges of  $\sim 1.63$  ‰ for  $\delta^{18}\text{O}$  and  $\sim 6.34$  ‰  
543 for  $\delta^2\text{H}$  for groundwater were much narrower than those found in GNIP records  
544 for the city of Faro (respectively  $\sim 8.43$  ‰ and  $\sim 57.3$  ‰). Nevertheless (Fig. 4a),  
545 the amount-weighted average isotope composition of precipitation inputs into  
546 the Ria Formosa catchment ( $\delta^{18}\text{O} = -4.8$  ‰ and  $\delta^2\text{H} = -27.13$  ‰) taken from the  
547 GNIP dataset (1978–2001) plots slightly above the Global Meteoric Water Line  
548 (GMWL, Clark and Fritz 1997) and below the Western Mediterranean Meteoric  
549 Water Line (WMMWL, Celle-Jeanton et al. 2001). In conjunction with the average  
550 isotopic composition of groundwater in the catchment, that of seawater  
551 (Carreira 1991) and adjacent coastal water, a precipitation-seawater mixing line  
552 (PP-SW Mix, Fig 4) may be defined ( $\delta^2\text{H} = 5.37 \times \delta^{18}\text{O} - 1.7$ ,  $r^2=0.99$ ). The slope of  
553 this mixing line is similar to that found by Munksgaard et al. (2012) for the Great  
554 Barrier Reef (i.e., 5.66). Additional relationships framing the isotopic  
555 composition of the waters in the catchment in  $\delta$ -space include the Local Meteoric  
556 Water Line (LMWL), defined by Carreira et al. (2005) as  $\delta^2\text{H} = (6.44 \pm 0.24) \times$   
557  $\delta^{18}\text{O} + (3.41 \pm 1.13)$  and the Eastern Mediterranean Meteoric Water Line  
558 (EMMWL, Gat and Carmi, 1970). This is introduced as an extreme boundary to  
559 the isotopic composition of precipitation in southern Portugal. Indeed, rain with  
560 high *d-excess* originating either from the eastern Mediterranean or aligned with  
561 extreme precipitation events might fall in the region (see Fig. 4c), particularly  
562 during summer and/or autumn (e.g., Frot et al. 2007).

563

#### 564 **4.2.2. $\delta^{18}\text{O}$ and $\delta^2\text{H}$ in groundwater**

565 In winter 2007, the stable isotope composition of groundwater in M12 reveals  
566 slight evaporative enrichment by comparison to the GMWL and LMWL, plotting  
567 along the precipitation seawater mixing line (Fig. 4b). The isotopic compositions  
568 of surface waters (WWTP settling lagoons and lagoon surface waters) and  
569 porewaters plotted between the LMWL and the PP-SW mixing line (Fig. 4b),  
570 suggesting their composition was controlled by the interplay between the  
571 mixture of sea and groundwater and evaporation–condensation cycles occurring  
572 along the hydrological travel path. In winter 2009 however, the range of isotopic

573 compositions of surface water samples ( $\sim 2.87$  ‰ for  $\delta^{18}\text{O}$  and  $\sim 3.96$  ‰ for  $\delta^2\text{H}$ )  
574 was significantly different (see inset, Fig. 4c). Their composition then fell  
575 between the WMMWL and the PP-SW mixing line. Even though the number of  
576 samples taken in winter 2007 was lower than those taken later and tide-specific  
577 sampling was absent, comparison of samples taken in both winters at high tide  
578 slack (Table S1; Stations 2, 3, 4, A and 3B) shows the isotopic composition of  
579 water in the Ramalhete and Faro channels was distinct — the observed  
580 difference in range cannot therefore be attributed to the sampling strategy.  
581 Groundwaters across the catchment could be divided into three distinct groups:  
582 samples from Pechão Gimno, Pechão Serra and Pechão Zona industrial (Table 2),  
583 all from unit M10, plot above the GMWL and the LMWL, while samples taken  
584 from the unconfined aquifer wells in the outer barrier islands belonging to the  
585 unconfined M12 aquifer (i.e., Deserta, Table S1), plot distinctly below the PP-SW  
586 mixing line. In between, M12 samples plot along (Ramalhete) and below the PP-  
587 SW Mixing line (Costa, Chelote, Rio Seco). Samples from unit M10 plot along a  
588 local evaporation line (LEL) with slope  $\sim 4.5$  while samples from unit M12,  
589 excluding the ones located within the Ria Formosa, plot along a LEL with slope  
590  $\sim 4.1$ .

#### 591 **4.2.3. Isotopic composition of beach porewater**

592 The pore water isotope compositions differed significantly between the winter of  
593 2007 and that of 2010/2011. Beach groundwater was sampled both during  
594 spring and neap tides from sediment depths ranging from 50 cm to 3.5 m below  
595 MTL across a beach profile from the upper to the lower intertidal during the  
596 latter period.  $\delta^{18}\text{O}$  ranged from 0.96 ‰ to -0.20 ‰ and  $\delta^2\text{H}$  from 2.5 ‰ to 8.5  
597 ‰ and plotted close to the LMWL (Fig. 5a) along an evaporation line defined by  
598  $\delta^2\text{H} = (4.02 \pm 0.56) \times \delta^{18}\text{O} + (4.51 \pm 0.31)$ ,  $n=24$ ,  $r^2=0.702$ , not shown). The slope  
599 of this LEL is slightly lower than those of the groundwater LELs (4.1 for the M12  
600 and 4.5 for the M10). The data fell into three distinct groups (Fig. 5a,b) according  
601 to the relative position of the sampling point within the beach section. The first  
602 group of samples (average  $\delta^{18}\text{O}$  of  $0.0 \pm 0.13$  ‰ and  $\delta^2\text{H}$  of  $3.5 \pm 0.93$  ‰,  $n=5$ )  
603 corresponded to the unsaturated and intermediate zones (upper intertidal),  
604 while the second (average  $\delta^{18}\text{O}$  of  $0.4 \pm 0.31$  ‰ and  $\delta^2\text{H}$  of  $6.1 \pm 0.47$  ‰,  $n=10$ )

605 and third groups (average  $\delta^{18}\text{O}$  of  $0.7 \pm 0.18$  ‰ and  $\delta^2\text{H}$  of  $8.0 \pm 0.37$  ‰,  $n=9$ )  
606 were isotopically heavier and included in that order pore water from the deeper  
607 (>2m below the surface) and shallower (<1m below the surface) areas of the  
608 beach section. The respective average pore water stable isotope compositions  
609 plotted close to the LMWL (Fig. 5a), showing enrichment in opposition to  
610 distance from the surface in the saturated zone and depletion in the unsaturated  
611 recharge zone, probably due to capillarity effects (Barnes and Allison 1988). The  
612 dependence of *d*-excess (Dansgaard 1964) on  $\delta^{18}\text{O}$  (Fig. 5b) illustrates the  
613 deviation of porewater composition from Craig's (1961b) GMWL ( $\delta^2\text{H} = 8 \times \delta^{18}\text{O}$   
614 +10) along significantly linear slopes dependent on local evaporation conditions.  
615 Indeed, porewater *d*-excess from deeper within the beach plots along the line  
616 defined by  $d = -6.7 (\pm 0.27) \times \delta^{18}\text{O} + 5.57 (\pm 0.13)$  ( $n=10$ ,  $r^2=0.987$ ,  $P<0.0001$ )  
617 while that from shallower areas plots along the line defined by  $d = -7.1 (\pm 0.69) \times$   
618  $\delta^{18}\text{O} + 7.28 (\pm 0.52)$  ( $n=9$ ,  $r^2=0.937$ ,  $P<0.0001$ ). These define slopes in  $\delta$ -space  
619 close to 1 and are consistent with the flow paths taken by beach groundwater  
620 between the seawater infiltration point at the higher beach face (higher *d*-excess)  
621 and the exfiltration point at the seepage face (lower *d*-excess). For the  
622 intermediate group of samples, longer flow paths (larger *d*-excess range) and less  
623 evaporative enrichment (lower average  $\delta^{18}\text{O}$ ) are consistent with tidal-forced  
624 circulation at larger depths within the beach face. Conversely, shorter flow paths  
625 (relatively narrow *d*-excess range) and more evaporative enrichment (higher  
626 average  $\delta^{18}\text{O}$ ) characterize shallower circulation pathways.

627 Interannual variability was also significant. The range of  $\sim 1.16$  ‰ for  $\delta^{18}\text{O}$  and  
628  $\sim 6.03$  ‰ for  $\delta^2\text{H}$  found in 2009–2011 was 50% and 36%, respectively, of the  
629 2007 range, in spite of a common sampling location. Furthermore, isotopic  
630 compositions for pore water collected in 2007 plotted in  $\delta$ -space clearly in  
631 between the LMWL and the PP-SW mixing line (Fig. 4b), while the 2010–2011  
632 samples overlap the LMWL (Figs. 4c and 5a). This occurs in spite of fewer  
633 samples being taken in 2007 and their depth of 50 cm below the surface, in  
634 contrast with the wide range of sediment depths sampled during 2009–2011.  
635 Paired ranges of pore water salinity also differ, varying between 21 and 36 in

636 2007 and between 36 and 43 in 2010 and 2011. These results suggest different  
637 water source functions were present during each sampling period.

#### 638 **4.2.4. Tidal variability of surface water $\delta^{18}\text{O}$ and $\delta^2\text{H}$**

639 Tides have a significant effect on the range of isotopic composition of surface  
640 water within the lagoon (see Fig. 6). In both lagoon sectors, the isotopic  
641 compositional range of water was much wider at low tide (Fig. 6a) than at high  
642 tide (Fig. 6b) but this variability was more apparent in the western sector.  
643 During low tide there  $\delta^2\text{H}$  ranged from 5.3 ‰ (Station 2B) to 7.9 ‰ (Station 2)  
644 and  $\delta^{18}\text{O}$  from -0.82 ‰ (Station 2B) to 2.05 ‰ (Station 3). By contrast,  $\delta^2\text{H}$   
645 ranged from 5.1 ‰ at Station 3B to 7.3 ‰ at 4B, while  $\delta^{18}\text{O}$  varied from -0.16 ‰  
646 (Station 4) to 0.86 ‰ (Station 1B and 2B). The water mass at Station 2B was  
647 most depleted in  $^{18}\text{O}$  during low tide (Fig. 6a) and the most enriched in  $^{18}\text{O}$   
648 during high tide (Fig. 6b) but remains at the lower end of the  $\delta^2\text{H}$  range covered  
649 by all collected samples during both tidal stages. Aspects of tide-induced  
650 circulation are also revealed when the western and eastern sectors are  
651 compared for identical tidal stages (Fig. 6a,b). During low tide (Fig. 6a), the  
652 isotope compositions of water collected at the Ramalhete channel and the  
653 associated Ancão basin (Stations 1B to 5B, Fig. 1) plot to the left of the LMWL,  
654 with the most isotopically depleted water found in Station 2B and the most  
655 enriched found at Station 1B. Conversely, water samples collected in the Faro  
656 channel (Stations 1 to 5) plot to the right of the LMWL. The situation is reversed  
657 during high tide (Fig. 6b), with isotopic compositions of water from Stations 1B  
658 to 4B plotting to the right of the LMWL, as a result of mixing with sea and coastal  
659 water and all others plotting to the left (mixing with internal lagoon water,  
660 including pore water).

661 Two mixing lines, [MX-1:  $\delta^2\text{H} = (0.97 \pm 0.08) \times \delta^{18}\text{O} + (5.70 \pm 0.09)$ ,  $r^2=0.871$ ,  
662  $n=21$ ; MX-2:  $\delta^2\text{H} = (1.02 \pm 0.12) \times \delta^{18}\text{O} + (7.13 \pm 0.10)$ ,  $r^2=0.842$ ,  $n=16$ ] and an  
663 evaporation line (LEL-1:  $\delta^2\text{H} = (3.88 \pm 0.26) \times \delta^{18}\text{O} + (3.26 \pm 0.27)$ ,  $r^2=0.969$ ,  
664  $n=9$ ) are defined by the paired  $\delta^{18}\text{O}$  and  $\delta^2\text{H}$  values of the surface and pore  
665 waters at low tide (Fig. 6a). The MX-1 line represents the isotopic composition of  
666 pore water taken from the deeper section (2–3.5 m below the sediment surface)

667 of the beach water table (Fig. 5) and surface waters from Station 2B in the  
668 Ramalhete Channel, the outer eastern sector locations in the lagoon (Stations A–  
669 E and J, Fig. 1) and water from the Faro channel (Stations 1–4, Fig. 1). The MX-2  
670 line represents the isotopic composition of pore water taken from the shallower  
671 section (0.5–1.5 m) below the sediment surface) of the beach water table (Fig. 5)  
672 and surface waters of the Ramalhete Channel (1B, Fig. 1), the Ancão channel  
673 close to the inlet (Stations 3B–5B, Fig. 1) and the landward stations of the  
674 eastern sector (Stations F–H, Fig. 1). LEL-1 describes all isotopic signatures of  
675 water collected in the eastern sector and intersects the LMWL amongst the most  
676 depleted pore water samples extracted from the beach (Fig. 6a) corresponding to  
677 the unsaturated zone. During high tide, water found at Stations A, B and C (Fig. 1)  
678 retains similar isotopic compositions (Fig. 6b) to the water mass found at the  
679 same locations during low tide (Fig. 6a).

680

## 681 **5. Discussion**

### 682 **5.1. Radon source attribution**

683 In order to derive an SGD rate for the Ria Formosa we divide the end-member  
684 source activity by the advective radon flux ( $4.14 \pm 3.00 \times 10^8$  Bq day<sup>-1</sup>) calculated  
685 from the mass balance. However, because radon budgets include <sup>222</sup>Rn sourced  
686 in seawater recirculation, the discharging fluid composition is important to  
687 discriminate between potential sources of SGD. In fact the two modes of SGD may  
688 be separated according to whether they drive a net influx of freshwater to the  
689 system (Santos et al. 2012). Indeed, there are three identified potential sources  
690 for advective radon input to the lagoon, i.e. Table 1, water in freshwater lenses  
691 under the outer barrier islands (outer reaches of the M12 aquifer) represented  
692 by the Deserta well (mean 0.95 salinity), porewater in sandy beaches (mean 40.6  
693 salinity) mobilized by tidal pumping (seawater recirculation), and finally,  
694 meteoric water travelling through the subterranean pathway (M12 aquifer),  
695 represented by samples taken from the Ramalhete borehole (mean 5.06 salinity).  
696 The corresponding volumetric discharges, if each of these potential sources is  
697 considered in turn to be the only source of SGD into the lagoon are  $4.42 (\pm 4.25)$   
698  $\times 10^6$  m<sup>3</sup> day<sup>-1</sup>,  $1.36 (\pm 1.28) \times 10^6$  m<sup>3</sup> day<sup>-1</sup> and  $6.26 (\pm 4.63) \times 10^4$  m<sup>3</sup> day<sup>-1</sup>,

699 corresponding respectively to  $\sim 3.16$ ,  $\sim 0.97$  and  $\sim 0.04\%$  of the mean daily flood  
700 prism ( $1.40 \times 10^8 \text{ m}^3$ ). When defining the radon source function, salinity is  
701 occasionally used as the discriminating parameter because of its conservative  
702 nature (Crusius et al. 2005; Swarzenski et al. 2006; Stieglitz et al. 2010). Yet, the  
703 low estimated SGD to tidal prism ratio combined with saline intrusion into the  
704 local aquifers (Silva et al. 1986; Table S1) advises against this option as the  
705 estimated discharge volumes would not have a discernable impact on the overall  
706 salinity of the Ria Formosa, leaving us without a way in which to verify the  
707 reliability of the choice. Furthermore, porewater salinity at the site where the  
708 piezometer transect is located (Fig. 1) was always very high ( $>35$ ; Table S1) but  
709 could be as low as 21 in 2007, suggesting different SGD modes might be active in  
710 different years. *So how do we confidently identify the source of radon?*

711 Our mass balances (see section 4.1.3) for each tidal stage suggest that radon is  
712 removed from the water column during the flood period. In the absence of any  
713 other realistic explanation we might accept that it had to be advected into the  
714 unsaturated intertidal zone during beach recharge. The daily flux of radon into  
715 unsaturated sandy sediments would then amount to  $16.25 \pm 13.5 \text{ Bq m}^{-2} \text{ day}^{-1}$ .  
716 Conversely, the input of radon into the water column during ebb was  $23.4 \pm 19.4$   
717  $\text{Bq m}^{-2} \text{ day}^{-1}$ . Because the mean radon inventory during high tide was  $19.3 \pm 4.74$   
718  $\text{Bq m}^{-3}$ , a flux of  $16.25 \pm 13.5 \text{ Bq m}^{-2} \text{ day}^{-1}$  into unsaturated sediments would  
719 equate to a beach recharge rate of  $\sim 1.2 \text{ m day}^{-1}$ . This figure is consistent with the  
720 discharge rates measured during 2006 by Leote et al. (2008) at the lower  
721 intertidal, which reached  $1.9 \text{ m day}^{-1}$ . If we therefore assume that beach  
722 discharge balances recharge on a volumetric basis at daily timescales, then the  
723 area of water infiltration would be  $\sim 1.13 \times 10^6 \text{ m}^2$ . Given the porosity of sandy  
724 beach sediments on site of  $\sim 0.3$ – $0.4$  (Rocha et al. 2009), recharge would only  
725 occur through about 7.5–10% of the maximum surface intertidal area of the  
726 lagoon (see section 2.1). Hence tidal pumping is a realistic explanation for the  
727 radon advected into the water column on a daily basis. Still, the radon data alone  
728 does not provide irrefutable proof that SGD estimated through the radon mass  
729 balance for June 2010 originates from seawater recirculation through beaches  
730 and pore water exchange mechanisms.



731 This proof is important: an example of how an unsupported choice of radon end  
732 member might significantly affect quantification of nitrate loading to the lagoon  
733 through SGD could be given at this stage to illustrate the effects of the lack of  
734 irrefutable source attribution. The mean nitrate concentration (in mg/L, spring  
735 tides, 2009 to 2011) was 0.1 for the lagoon water column, 0.81 for beach pore  
736 waters, 2.22 in the Deserta well, and 130 for the Campina de Faro aquifer (M12).  
737 Our discharge estimates based on the radon balance, would then result in  
738 potential average SGD borne nitrate loading to the Ria Formosa of 0.96, 9.8 and  
739 8.14 Tons N day<sup>-1</sup>, if the source of excess radon was respectively seawater  
740 recirculation through beach sands or fresh groundwater originating from either  
741 the lens under the dune cordon or the landward section of M12 aquifer. Two  
742 cautionary notes on these numbers should be obvious: (a) the latter would drive  
743 net N additions to the lagoon water budget while the former would not, implying  
744 that (b) the loadings based on directly multiplying fresh SGD by the average  
745 nutrient concentrations found in the end member samples ignore any  
746 transformations occurring within the interface before the mixture arrives at the  
747 lagoon proper, and therefore are likely to be overestimated.

748 Ferreira et al. (2003) estimated total N fluxes to the lagoon at 1028 Tons N/y  
749 (2.82 Tons N day<sup>-1</sup>), with 58% (1.64 Ton N day<sup>-1</sup>) originating from diffuse  
750 sources. Simple extrapolation from our data would suggest that ~34% of the  
751 total N fluxes to the lagoon, and ~59% of the non-point source loading, would  
752 arise from seawater recirculation through beaches, while the meteoric SGD  
753 sources would multiply the total N loading into the system by a factor of 6 or 5  
754 on a daily basis, depending on the composition of fresh groundwater. These two  
755 latest figures compound our cautionary notes above. Furthermore, during winter  
756 2010 and 2011, when pore water salinities were very high, nitrate available in  
757 pore waters at the littoral fringe was likely sourced from benthic mineralization  
758 of local organic matter (autochthonous source) and not in fresh groundwater  
759 input. Conversely, because nitrate contamination of the Campina de Faro aquifer  
760 is anthropogenic, freshwater inflow via SGD into the lagoon would also define  
761 the associated nitrate inputs as allochthonous, or “new” contributions to the  
762 system’s nutrient budget. Depending on SGD source therefore, there would be an

763 order of magnitude difference between allochthonous and autochthonous  
764 sources of nitrate into the lagoon, even if the former might be overestimated as  
765 discussed. Accurately identifying the SGD source function would therefore be  
766 absolutely necessary to understand the biogeochemical workings of the lagoon,  
767 but this is not possible with the radon data alone, even in combination with the  
768 salinity data.

769 However, the stable isotope signatures of surface water bring clarity to the  
770 problem. The Local Evaporation Line (LEL-1, Fig. 6a) fitted by linear regression  
771 of the samples taken within the eastern sector at low tide intersects the LMWL  
772 close to the average isotopic signature of beach pore water in the unsaturated  
773 zone (Figs. 5a and 6a). This indicates the original composition of the surface  
774 water before evaporation and mixing takes place within the lagoon. The origin of  
775 the surface water is the recharge into the unsaturated beach area, which then  
776 reveals isotopic enrichment in proportion to its permanence within the system  
777 and the consequent extent of evaporative loss. Indeed, water in the upper  
778 intertidal at low tide will see its isotopic signature depleted within the  
779 sedimentary matrix — in the unsaturated zone, the isotopic concentration  
780 decreases quickly from a maximum at the zone of evaporation (phreatic surface)  
781 within the sediment matrix to a minimum close to the surface because of the  
782 movement of water vapor through the pores toward the surface (Barnes and  
783 Allison 1983, 1988). While this is clear for the eastern sector, within the western  
784 sector there is another surface source of water (WWTP) that further complicates  
785 the picture. This water joins the lagoon close to Station 2B (Fig. 6a). So, the pore  
786 water in the unsaturated sediments mixes over time with the lagoon recharge at  
787 high tide and water already present within the tidal wedge (c.f. Robinson et al.  
788 2007), whereupon it leaves during beach discharge at low tide, either through  
789 shallow or deeper flow paths (Fig. 5b) and mixes with other meteoric sources  
790 and seawater (MX-1, MX-2, Fig. 6a).

791 For the period between the winter of 2009 and that of 2010/2011 therefore, the  
792 combined stable isotope and radon tracer approach allows definite attribution of  
793 the SGD source into the Ria Formosa. SGD arises from seawater recirculation  
794 through the permeable beach sediments of the lagoon driven by the tide. In the

795 absence of meteoric SGD inputs, a significant amount of the tidal prism (~1%)  
796 circulates through local sandy sediments driven by tidal pumping, at a rate of  
797  $\sim 1.4 \times 10^6 \text{ m}^3 \text{ day}^{-1}$ . This implies that the entire tidal-averaged volume of the  
798 lagoon ( $140 \times 10^6 \text{ m}^3$ ) is filtered through its sandy beaches within 100 days, or  
799 about 3.5 times a year. Based on our nutrient data, the average nitrate loading  
800 driven by this SGD mode to the Ria Formosa can now be confidently put at an  
801 average of  $0.96 \text{ Ton N day}^{-1}$ , ~59% of the non-point source nitrogen loading  
802 estimated by Ferreira et al. (2003).

803 Salinity (see Table S1) does not correlate well with both  $\delta^{18}\text{O}$  and  $\delta^2\text{H}$ , though,  
804 particularly for samples with  $\delta^{18}\text{O} > 1 \text{ ‰}$  and/or  $\delta^2\text{H} > 1 \text{ ‰}$  and  $S > 37 \text{ ‰}$ . With  
805 reference to surface water  $\delta^{18}\text{O}$  values these comprise the most isotopically  
806 enriched waters found during low tide respectively the innermost stations in the  
807 eastern sector (Stations G, H and F; Figs. 1 and 6a) and at locations within the  
808 Faro channel (Stations 1–4; Figs. 1 and 6a) as discussed earlier. It is also the case  
809 for most pore water samples. Indeed, even if the mean composition of pore-  
810 water from different sections of the beach plots along well-defined mixing and  
811 evaporation lines (Fig. 5a,b), the average salinities of each group do not change  
812 significantly with  $\delta^{18}\text{O}$  enrichment ( $40.2 \pm 1.78$ ,  $40.6 \pm 2.57$  and  $40.6 \pm 2.07$   
813 respectively). While this observation is consistent with theory (Craig and Gordon  
814 1965) and previous analysis on the covariance of  $\delta^{18}\text{O}$ ,  $\delta^2\text{H}$  and salinity in  
815 seawater (Rohling 2007), it also implies that the joint use of these tracers to infer  
816 the relative contribution of different source functions has to be done with care in  
817 semi-confined coastal water bodies subject to significant evaporation. As further  
818 support to this observation, we note that the mixing lines (MX-1 and MX-2, Fig 6  
819 a) between the pore-water within the beach tidal wedge and the most enriched  
820 waters found in the western sector ( $\delta^2\text{H} = (0.97 \pm 0.08) \times \delta^{18}\text{O} + (5.70 \pm 0.09)$ ,  
821  $r^2=0.87$ ,  $n=21$ ) and between the Ramalhete Channel and Ancão Basin (Stations  
822 3B, 4B, 5B) and the water mass near Olhão at Stations G and H ( $\delta^2\text{H} = (1.02 \pm$   
823  $0.18) \times \delta^{18}\text{O} + (7.13 \pm 1.01)$ ,  $r^2=0.84$ ,  $n=16$ ) are virtually the same as that  
824 characteristic of the modern surface ocean ( $\delta^2\text{H} = 1.05 \times \delta^{18}\text{O} + 6.24$ ,  $r^2=0.21$ ,  
825  $n=62$ ) within a comparable salinity range (Rohling 2007). This observation  
826 suggests in coastal ocean regions and areas of restricted exchange like lagoons,

827 the stable isotope signature of seawater reflects important contributions arising  
828 from pore-water exchange driven by tidal pumping, amongst other mechanisms.  
829 Identifying and discriminating these contributions brings insights also into the  
830 hydrological paths active within these systems and therefore provides an  
831 invaluable tool to support reliable biogeochemical budgets.

832

## 833 **5.2. Hydrological pathways and dispersion of SGD in the Ria Formosa** 834 **Lagoon**

835 The amount-weighted isotopic composition of precipitation over Faro (GNIP:  
836 IAEA/WMO, 2013) plots (Fig. 4a) at the intercept point of the GMWL, the LMWL  
837 (slope ~6.4) and the precipitation-seawater mixing line (slope ~5.4). The  
838 isotopic signature of precipitation hence plots close to that of groundwater,  
839 indicating that local aquifers are directly recharged by precipitation, in  
840 agreement with prior reports (Engelen and van Beers 1986). The isotopic  
841 composition of surface waters also reveals that the lagoon and the adjacent  
842 coastal water may be classified as a coastal boundary zone similar to that  
843 described elsewhere (Blanton et al. 1989; Blanton et al. 1994; Moore 2000), in  
844 which the isotopic signatures result from the mixing between offshore seawater  
845 and continental meteoric sources affected by surface evaporation.

846 Accordingly (Fig. 6), the stable isotope composition of water within the lagoon  
847 varies with tidal stage and will be affected on the one hand by the magnitude,  
848 origin and pathways taken by the meteoric inputs and on the other by internal  
849 mixing, driven by lagoon hydrodynamics and by the local evaporation regime.  
850 Nevertheless, the pore water end-member is part of the surface water mixture  
851 on both sampled periods, although in different ways: some pore waters (Pw<sub>e</sub>  
852 and Pw<sub>f</sub>; see Table 2) collected at the same site were significantly more  
853 depleted in both <sup>18</sup>O and <sup>2</sup>H during 2007 (Fig. 4b) when compared to 2009–2011  
854 (Fig. 4c) and these are characterized by comparatively low salinities (21 and 23,  
855 Table 2). Station 2B is the closest to the Faro WWTP outlet; during low tide the  
856 water mass joining the lagoon mixture there has an isotopic signature close to  
857 the Western Mediterranean Water Line (Fig. 6a), suggesting that a meteoric

858 source of water joins the lagoon there presumably as part of the WWTP  
859 discharge. On the other hand, the exchange in position of the isotopic signature  
860 of water at Stations 1–5 and 1B–3B with reference to the LMWL in  $\delta^{18}\text{O} - \delta^2\text{H}$   
861 space during flood (Fig. 6b) suggests a hydrodynamic connection between the  
862 Ramalhete Channel, the Ancão inlet and the water masses on the eastern sector.  
863 This connection would occur via the Faro-Olhão inlet and associated channels as  
864 ebb progresses onto flood, linking both the stations closest to the city of Olhão  
865 (Stations E, F, G) and the ones closer to the coastal ocean (Stations A, B, C), to the  
866 water masses originally present in the western sector. Indeed, Stations 1 to 4 in  
867 the Faro channel display depletion of  $^{18}\text{O}$  during high tide (Fig. 6b) by  
868 comparison to low tide (Fig. 6a). This provides evidence that the meteoric source  
869 present within the Ramalhete channel also influences the water in the Faro  
870 channel during high tide. Furthermore, the isotopic data suggest that part of the  
871 water mass out flowing through the Ramalhete channel during ebb tide (Stations  
872 2B–5B) eventually end up being present at Stations F, G and H close to the city of  
873 Olhão via the inner portion of the system (Station 1B), having mixed with  
874 shallow beach groundwater (MX-2 in Fig. 6a) while water from the same region  
875 might also be led to Stations A, B and C in the eastern sector via Station 5 after  
876 mixing through the beach water table (MX-1 in Fig. 6a,b). The dominant  
877 alongshore drift in the area is eastward, and in fact, Pacheco et al. (2010) show  
878 that a strong hydraulic connection exists between the the Ancão, Barra Nova  
879 (Faro-Olhão) and Armona (Barra Velha) inlets, whereby the excess flood prism  
880 at Barra Nova is directed toward both the Ancão and the Armona ebb-dominated  
881 inlets. The combination of data indicates that the body of water ebbing in the  
882 first instance through the Ramalhete channel is partially retained within the  
883 system and ends up in the Faro channel before the subsequent flood moves it  
884 eastward, either via an internal pathway eastward from the Ancão inlet basin  
885 and/or externally, looping back into the lagoon via the Faro-Olhão inlet after  
886 exiting through the Ancão inlet (Fig. 6a,b).

887 The combination of flood lag-time between the Ancão and Barra Nova inlets, the  
888 eastward alongshore drift and the meteoric source of water at the WWTP plant  
889 outlet (closest to Station 2B) creates the characteristic inversion observed in

890  $\delta^{18}\text{O}$ - $\delta^2\text{H}$  relationships and highlighted in Fig. 6a,b. This circulation path inferred  
891 from the isotopic composition of water is also consistent with the radon data,  
892 since the radon enriched water masses found in the Ramalhete and Faro  
893 channels (Fig. 2a) during low tide would eventually be transported toward the  
894 eastern sector via the distribution of the excess flood prism at Faro-Olhão  
895 (Pacheco et al. 2010). This would help explain why the radon inventory in the  
896 eastern sector is higher during flood tide (Fig. 2b), and why the net exchange of  
897 radon is directed into the lagoon at both Quatro-Águas and Barra Nova (Table 1),  
898 as part of the radon associated with beach seepage would be retained in the  
899 lagoon and/or transported back into the system via the Barra-Nova after exiting  
900 through the Ancão inlet.

901

### 902 **5.3. Inter-annual comparison of lagoon hydrology using Deuterium** 903 **excess**

904 Because of the relatively higher enrichment in  $^{18}\text{O}$  compared to  $^2\text{H}$  in the residual  
905 water (Gat 1996), deuterium excess ( $d$ -excess =  $d = \delta^2\text{H} - 8 \times \delta^{18}\text{O}$ ) decreases in  
906 water as evaporation progresses (i.e., as  $\delta^{18}\text{O}$  increases). It follows therefore that  
907 a plot of  $d$ -excess versus  $\delta^{18}\text{O}$  (in a similar fashion to Fig. 5b for pore water) might  
908 reveal the path taken by a particular water mass within a catchment area,  
909 because, (a) the magnitude of the fractionation imposed by evaporation along  
910 the travel path affects the  $d$ -excess of residual water (setting the slope of paired  
911  $d$ - $\delta^{18}\text{O}$  relationships), and (b) water of different origins would have different  $d$ -  
912 excess values. The slope of the  $d$ - $\delta^{18}\text{O}$  covariance line shows the deviation of  
913 isotopic compositions from Craig's meteoric water line (Craig 1961b). Therefore  
914 its magnitude in absolute terms is proportional to the extent of evaporative  
915 enrichment, a function of the exposure time of the water to evaporation.  
916 Conversely, following the line along decreasing  $\delta^{18}\text{O}$  values would lead us to the  
917 original isotopic composition of the water, set before the evaporative regime  
918 changed. These characteristics allow us to disentangle and identify the main  
919 hydraulic pathways active in the Ria Formosa and compare the two periods

920 under scrutiny to reveal the distinct nature of SGD within the system (Figs. 5b  
921 and 7a,b).

922 Accordingly, four significant  $d$ - $\delta^{18}\text{O}$  correlation lines are identified in the basin  
923 (Fig. 7). In 2007, two pathways (P1 and P2) connecting the composition of M12  
924 groundwater with water sampled in the lagoon are revealed: P1, with  $d = (-1.10$   
925  $\pm 0.02) \times \delta^{18}\text{O} + (4.41 \pm 0.1)$ ,  $r^2=0.997$ ,  $n=6$ ,  $P\sim 0$ ; and P2, with  $d = (-1.85 \pm 0.05) \times$   
926  $\delta^{18}\text{O} + (0.72 \pm 0.11)$ ,  $r^2=0.992$ ,  $n=14$ ,  $P\sim 0$ . These relations reveal the two  
927 different pathways into the Ria followed by groundwater from the M12 aquifer  
928 in 2007 (Fig. 7a). The surface water circulation pathway (P1) originates when  
929 water from the public supply (sourced in local aquifers) is treated at the WWTP  
930 and subsequently discharged into the lagoon, whereupon it circulates into the  
931 Ancão basin mixing with coastal and seawater. This pathway is consistent with  
932 the internal circulation path discussed earlier. In contrast, the groundwater  
933 pathway (P2) followed by water originating in the same aquifer crosses the  
934 subterranean estuary and emerges later ( $d$ - $\delta^{18}\text{O}$  correlation slope magnitude is  
935 higher than P1) within the lagoon where it mixes with surface waters, including  
936 seawater and the WWTP outlet emissions (Fig. 7a). Hence the isotope data  
937 conclusively show two aspects of the local water balance in 2007: on the one  
938 hand, water for public consumption was essentially extracted from groundwater  
939 sources while on the other SGD into the lagoon comprising a net water input into  
940 the system was present.

941 The situation later (2009–2011) was substantially different (Fig. 7b). Two major  
942 hydraulic pathways are shown in the isotopic data (P3, P4); P3, with  $d = (-7.8 \pm$   
943  $1.2) \times \delta^{18}\text{O} - (22.76 \pm 5.04)$ ,  $r^2=0.813$ ,  $n=10$ ,  $P=0.0002$ ; and P4,  $d = (-7.43 \pm 0.18)$   
944  $\times \delta^{18}\text{O} + (6.45 \pm 0.18)$ ,  $r^2=0.979$ ,  $n=37$ ,  $P\sim 0$ . These highlight other aspects of the  
945 local water balance. Firstly, P3 suggests that groundwater from the M10 aquifer  
946 mixes with water in M12, and that the local groundwater flow follows a  
947 Northeast to southeast general direction (*c.f.* location of M10 and M12 in Fig. 1),  
948 eventually communicating under the Ria Formosa with freshwater lenses  
949 present in the barrier islands, where the  $d$ -*excess* signature of groundwater is  
950 lowest. Secondly, P4 shows that water used for public consumption in the  
951 catchment was mainly withdrawn from a direct meteoric source (position of

952 rainwater signature, Fig. 7b). This water, upon leaving the WWTPs then mixes  
953 with surface and re-circulated seawater establishing the mixing line for the  
954 lagoon (Figs. 6a and 7b). It is also evident that the surface water samples  
955 collected in the lagoon in 2007 plot close to the P4 line, suggesting that the  
956 magnitudes of the factors driving evaporation and internal circulation in the  
957 lagoon are generally stable on a multiannual basis. This comparative approach  
958 confirms, additionally, that the subterranean pathway was not present in 2009–  
959 2011, and hence SGD at this time was comprised entirely of saline water re-  
960 circulated through the sandy beaches by tidal pumping.

961 The difference observed in water sources for public water supply and their  
962 isotopic signature in the catchment and subsequently released through the  
963 WWTPs into the lagoon is consistent with the changes occurring in the regional  
964 water management strategy: while water to meet irrigation and public  
965 consumption demand relied almost entirely on groundwater abstraction until  
966 the 2000's (Stigter et al. 2006), from this period onwards it was to be drawn  
967 almost exclusively from surface reservoirs North of the littoral zone. However, a  
968 substantial number of the local groundwater captions remained active in support  
969 of irrigation, while some of the major municipal captions had to be re-activated  
970 after the 2005 drought (EM-DAT 2013) to support consumption demand when  
971 surface reservoirs became depleted. In fact, because of the unpredictability of  
972 scarcity periods, the current operational thinking tends toward mixing both  
973 water sources to face demand, with the primary source being surface water  
974 reservoirs (Monteiro and Costa Manuel 2004; Stigter and Monteiro 2008). Our  
975 approach clearly indicates that this is the case for 2009–2011 as the WWTP plant  
976 water signal shows the water being discharged as meteoric in origin (Figs. 6a  
977 and 7b). Following the implementation of a mixed source water supply chain, the  
978 activity of the SGD subterranean pathway into the Ria becomes dependent on  
979 whether groundwater levels in M12 are sufficient to establish a hydraulic  
980 gradient driving the flow as was apparently the case in 2007 (Fig. 7a). Increased  
981 water mining and reduced aquifer recharge would provide the counterbalance  
982 by reducing groundwater levels and consequently the hydraulic gradient driving  
983 SGD of meteoric origin into the system via the subterranean estuary.



## 984 6. Concluding Remarks

985 We compared hydrological scenarios in a semi-arid coastal lagoon across two  
986 different periods, aiming to distinguish SGD modes and correctly identify end-  
987 member contributions to the water mixture within the system. While it has been  
988 established that radon mass conservation allows for the determination of total  
989 SGD, i.e., meteoric plus re-circulated water flow, we show that combining this  
990 information with stable isotope hydrology contributes to define and distinguish  
991 origins and pathways followed by SGD into the system. While  $\delta^{18}\text{O}$  and *d-excess*  
992 paired data helped define the active hydrological pathways in the Ria Formosa,  
993  $\delta^2\text{H}$  versus  $\delta^{18}\text{O}$  plots provided insights into water source functions and their  
994 dispersion through the lagoon. Using our combined approach, SGD occurring in  
995 the Ria Formosa could be separated into a discharge incorporating net meteoric  
996 water input into a receiving ecosystem (2007) and an input with no net water  
997 transfer (2009–2011). We conclude that whilst the Ria Formosa receives SGD  
998 through tidal pumping (as in 2009–2011), it is also occasionally subject to SGD  
999 inputs of meteoric origin (as in 2007) directly associated with the contaminated  
1000 M12 aquifer.

1001 In the absence of meteoric SGD inputs part of the tidal prism (1.3%) circulates  
1002 through local sandy sediments driven by tidal pumping, at a rate of  $\sim 1.4 \times 10^6 \text{ m}^3$   
1003  $\text{day}^{-1}$ . This implies that the entire tidal-averaged volume of the lagoon ( $140 \times 10^6$   
1004  $\text{m}^3$ ) is filtered through its sandy beaches within 100 days, or about 3.5 times a  
1005 year, driving an estimated load of  $\sim 350 \text{ Ton N y}^{-1}$  into the lagoon. Conversely,  
1006 using the estimates for the upper bound of N concentration found in the  
1007 freshwater component of SGD during 2006 ( $0.4 \text{ mmol L}^{-1}$ ) and the associated  
1008 SGD-borne freshwater discharge of  $\sim 1.1 \times 10^7 \text{ m}^3 \text{ y}^{-1}$  estimated by Leote et al.  
1009 (2008) based on seepage meter measurements, meteoric SGD inputs could add a  
1010 further  $\sim 61 \text{ Ton N y}^{-1}$  to the lagoon. If for the former the source is autochthonous  
1011 and responsible for a rather large fraction (59%) of the estimated nitrogen  
1012 inputs into the system via non-point sources (Ferreira et al. 2003), leaving no  
1013 direct mitigation options in the context of environmental management — it isn't  
1014 so for the latter, as specific measures could be implemented in support of  
1015 mitigation (e.g., Almasri and Kaluarachchi 2004). Nevertheless, the potential

1016 loadings delivered from two distinct vectors differ in magnitude, frequency and  
1017 origin, and could therefore cause different ecosystem-level impacts. Hence while  
1018 simple or weighted averages of end member radon activities might be useful  
1019 under well defined circumstances (Crusius et al. 2005; Swarzenski et al. 2006;  
1020 Kroeger et al. 2007; Blanco et al. 2011) in radon budgets to evaluate SGD as a  
1021 potential pollutant source in comparison to other vectors (local surface drainage,  
1022 riverine input, etc), these are of little value to effectively provide environmental  
1023 managers with the causal chain alluded to in the introduction: without actual  
1024 source identification and attribution, there is little that can be done to manage  
1025 potential pollutant loading of coastal ecosystems via SGD.

1026

## 1027 **Acknowledgements**

1028 Funding for this study was provided by the Portuguese Foundation for Science and  
1029 Technology (FCT), the EU (FEDER) and the Portuguese Government through project  
1030 NITROLINKS - “NITROgen loading into the Ria Formosa through Coastal  
1031 Groundwater Discharge (CGD) - Pathways, turnover and LINKS between land and  
1032 sea in the Coastal Zone” (PTDC/MAR/70247/2006). JW was funded by the  
1033 Environmental Protection Agency (EPA) Ireland under the STRIVE initiative (project  
1034 code 2008-FS-W-S5). JS acknowledges the support provided by the FP7 EU Marie  
1035 Curie Career Integration Grant (grant PCIG09-GA-2011-293499). Numerous people  
1036 helped at various stages of the work. In particular, the authors wish to thank Ms Inês  
1037 Rio, Ms Rachel Kilgallon, Mr Collin Snowberg, Ms Sinead Kehoe and Ms Aine  
1038 Kenny, for their help with the field surveys and laboratory analysis. The pilots of our  
1039 survey boats, Mr Daniel Machado, Mr Pedro Barroso and the Animaris crews are  
1040 gratefully acknowledged – their profound knowledge of the system and their piloting  
1041 proficiency made the impossible possible.

1042

1043

1044 **References**

1045

1046 Almasri, M. N. and Kaluarachchi, J. J.: Assessment and management of long-term  
1047 nitrate pollution of ground water in agriculture-dominated watersheds, *J. Hydrol.*,  
1048 295, 225–245, 2004.

1049

1050 Almeida, C. and Silva, M. L.: Incidence of agriculture on water quality at Campina de  
1051 Faro (south Portugal), in: *Hidrogeologia-y-Recursos-Hidraulicos*, vol. 12,  
1052 Asociacion Españolade Hidrologia Subterranea, Madrid, Spain, 249 – 257, 1987.

1053

1054 Almeida, C. J., Mendonca, J. J. L., Jesus, M. R., and Gomes, A. J.: *Sistemas aquiferos*  
1055 *de Portugal Continental (Aquifer Systems of Continental Portugal)*, Instituto Nacional  
1056 da Água – INAG, Lisbon, 2000.

1057

1058 Balouin, Y.: *Les embouchures mésotidales (tidal inlets) et leur relation avec les*  
1059 *littoraux adjacents – exemple de la Barra Nova, sud Portugal*, PhD thesis, University  
1060 of Bordeaux, Bordeaux, 2001.

1061

1062 Barnes, C. J. and Allison, G. B.: The distribution of deuterium and  $^{18}\text{O}$  in dry soils: 1.  
1063 Theory, *J. Hydrol.*, 60, 141–156, 1983.

1064

1065 Barnes, C. J. and Allison, G. B.: Tracing of water movement in the unsaturated zone  
1066 using stable isotopes of hydrogen and oxygen, *J. Hydrol.*, 100, 143–176, 1988.

1067

1068 Beck, A. J., Tsukamoto, Y., Ovar-Sanchez, A., Huerta-Diaz, M., Bokuniewicz, H. J.,  
1069 and Sañudo-Wilhelmy, S. A.: Importance of geochemical transformations in  
1070 determining submarine groundwater discharge-derived trace metal and nutrient  
1071 fluxes, *Appl. Geochem.*, 22, 477–490, 2007.

1072

1073 Blanco, A. C., Watanabe, A., Nadaoka, K., Motooka, S., Herrera, E. C., and  
1074 Yamamoto, T.: Estimation of nearshore groundwater discharge and its potential  
1075 effects on a fringing coral reef, *Mar. Pollut. Bull.*, 62, 770–785, 2011.

1076

1077 Blanton, J. O., Amft, J., Oey, L.-Y., and Lee, T. N.: Advection of momentum and  
1078 buoyancy in a coastal frontal zone, *J. Phys. Oceanogr.*, 19, 98–115, 1989.

1079

1080 Blanton, J. O., Werner, F., Kim, C., Atkinson, L., Lee, T., and Savidge, D.: Transport  
1081 and fate of low-density water in a coastal frontal zone, *Cont. Shelf. Res.*, 14, 401–427,  
1082 1994.

1083

1084 Bratton, J. F.: The three scales of submarine groundwater flow and discharge across  
1085 passive continental margins, *J. Geol.*, 118, 565–575, 2010.

1086

1087 Burnett, W. C. and Dulaiova, H.: Estimating the dynamics of groundwater input into  
1088 the coastal zone via continuous radon-222 measurements, *J. Environ. Radioactiv.*, 69,  
1089 21–35, 2003.

1090

1091 Burnett, W. C., Taniguchi, M., and Oberdorfer, J.: Measurement and significance of  
1092 the direct discharge of groundwater into the coastal zone, *J. Sea Res.*, 46, 109–116,

1093 2001a.  
1094  
1095 Burnett, W. C., Kim, G., and Lane-Smith, D.: A continuous monitor for assessment of  
1096 <sup>222</sup>Rn in the coastal ocean, *J. Radioanal. Nucl. Ch.*, 249, 167–172, 2001b.  
1097  
1098 Burnett, W. C., Bokuniewicz, H., Huettel, M., Moore, W. S., and Taniguchi, M.:  
1099 Groundwater and pore water inputs to the coastal zone, *Biogeochemistry*, 66, 3–33,  
1100 2003.  
1101  
1102 Burnett, W. C., Aggarwal, P. K., Aureli, A., Bokuniewicz, H., Cable, J. E., Charette,  
1103 M. A., Kontar, E., Krupa, S., Kulkarni K. M., Loveless, A., Moore, W. S., Oberdorfer,  
1104 J. A., Oliveira, J., Ozyurt, N., Povinec, P., Privitera, A. M., Rajar, R., Ramessur, R.  
1105 T., Scholten, J., Stieglitz, T., Taniguchi, M., and Turner, J. V.: Quantifying submarine  
1106 groundwater discharge in the coastal zone via multiple methods, *Sci. Total Environ.*,  
1107 367, 498–543, 2006.  
1108  
1109 Burnett, W. C., Peterson, R., Moore, W. S., and de Oliveira, J.: Radon and radium  
1110 isotopes as tracers of submarine groundwater discharge – results from the Ubatuba,  
1111 Brazil SGD assessment intercomparison, *Estuar. Coast. Shelf S.*, 76, 501–511, 2008.  
1112  
1113 Cable, J. E., Burnett, W. C., Chanton, J. P., and Weatherly, G. L.: Estimating  
1114 groundwater discharge into the northeastern Gulf of Mexico using radon-222, *Earth  
1115 Planet. Sc. Lett.*, 144, 591–604, 1996.  
1116  
1117 Cable, J. E., Martin, J. B., Swarzenski, P. W., Lindenberg, M. K., and Steward, J.:  
1118 Advection within shallow pore waters of a coastal lagoon, Florida, *GroundWater*, 42,  
1119 1011–1020, 2004.  
1120  
1121 Carpenter, S. R., Caraco, N. F., Correll, D. L., Howarth, R. W., Sharpley, A. N., and  
1122 Smith, V. H.: Nonpoint pollution of surface waters with phosphorus and nitrogen,  
1123 *Ecol. Appl.*, 8, 559–568, 1998.  
1124  
1125 Carreira, P. M.: Mechanisms of Salinization of Coastal Aquifers in the Algarve, MSc  
1126 thesis, ICEN/INETI, 143 pp., 1991.  
1127  
1128 Carreira, P. M., Araújo, M. F., and Nunes, D.: Isotopic composition of rain and water  
1129 vapour samples from Lisbon region: characterization of monthly and daily events, in:  
1130 *Isotopic Composition of Precipitation in the Mediterranean Basin in Relation to Air  
1131 Circulate Patterns and Climate*, IAEA-TECDOC-1453, IAEA, Vienna, Austria, 141–  
1132 156, 2005.  
1133  
1134 Celle-Jeanton, H., Travi, Y., and Blavoux, B.: Isotopic typology of the precipitation in  
1135 the western Mediterranean region at three different time scales, *Geophys. Res. Lett.*,  
1136 28, 1215–1218, 2001.  
1137  
1138 Charette, M. A. and Sholkovitz, E. R.: Trace element cycling in a subterranean  
1139 estuary: Part 2. Geochemistry of the pore water, *Geochim. Cosmochim. Acta*, 70,  
1140 811–826, 2006.  
1141  
1142 Charette, M. A., Sholkovitz, E. R., and Hansel, C. M.: Trace element cycling in a

1143 subterranean estuary: Part 1. Geochemistry of the permeable sediments, *Geochim.*  
1144 *Cosmochim. Acta*, 69, 2095–2109, 2005.

1145

1146 Church, T. M.: An underground route for the water cycle, *Nature*, 380, 579–580,  
1147 1996.

1148

1149 Clark, I. D. and Fritz, P.: *Environmental Isotopes in Hydrogeology*, CRC Press, Boca  
1150 Raton, Florida, 1997.

1151

1152 Colbert, S. L. and Hammond, D. E.: Temporal and spatial variability of radium in the  
1153 coastal ocean and its impact on computation of nearshore cross-shelf mixing rates,  
1154 *Cont. Shelf. Res.*, 27, 1477–1500, 2007.

1155

1156 Colbert, S. L. and Hammond, D. E.: Shoreline and seafloor fluxes of water and short-  
1157 lived Ra isotopes to surface water of San Pedro Bay, CA, *Mar. Chem.*, 108, 1–17,  
1158 2008.

1159

1160 Colbert, S. L., Hammond, D. E., and Berelson, W. M.: Radon-222 budget in Catalina  
1161 Harbor, California: 1. Water mixing rates, *Limnol. Oceanogr.*, 53, 651–658, 2008a.

1162

1163 Colbert, S. L., Berelson, W. M., and Hammond, D. E.: Radon-222 budget in Catalina  
1164 Harbor, California: 2. Flow dynamics and residence time in a tidal beach, *Limnol.*  
1165 *Oceanogr.*, 53, 659–665, 2008b.

1166

1167 Corbett, D. R., Burnett, W. C., Cable, P. H., and Clark, S. B.: A multiple approach to  
1168 the determination of radon fluxes from sediments, *J. Radioanal. Nucl. Ch.*, 236, 247–  
1169 253, 1998.

1170

1171 Craig, H.: Standard for reporting concentrations of deuterium and oxygen-18 in  
1172 natural waters, *Science*, 133, 1833–1834, 1961a.

1173

1174 Craig, H.: Isotopic variations in meteoric waters, *Science*, 133, 1702–1703, 1961b.

1175

1176 Craig, H. and Gordon, L. I.: Deuterium and oxygen-18 variations in the ocean and the  
1177 marine atmosphere, in: *Proceedings of a Conference on Stable Isotopes in*  
1178 *Oceanographic Studies and Paleotemperatures*, Spoleto, Italy, edited by: Tongiorgi,  
1179 E., 9–130, 1965.

1180

1181 Crusius, J., Koopmans, D., Bratton, J. F., Charette, M. A., Kroeger, K., Henderson, P.,  
1182 Ryckman, L., Halloran, K., and

1183

1184 Colman, J. A.: Submarine groundwater discharge to a small estuary estimated from  
1185 radon and salinity measurements and a box model, *Biogeosciences*, 2, 141–157,  
1186 doi:10.5194/bg-2-141-2005, 2005.

1187

1188 Dansgaard, W.: Stable isotopes in precipitation, *Tellus*, 16, 436–468, 1964.

1189

1190 Dias, J. M. and Sousa, M. C.: Numerical modeling of Ria Formosa tidal dynamics, *J.*  
1191 *Coast. Res.*, 56, 1345–1349, 2009.

1192

1193 Edmunds, W. M.: Renewable and non-renewable groundwater in semi-arid and arid  
1194 regions, in: *Developments in Water Science*, Vol. 50, edited by: Alsharhan, A. S. and  
1195 Wood, W. W., Elsevier, Amsterdam, 265–280, 2003.

1196  
1197 EM-DAT: The OFDA/CRED International Disaster Database, available at:  
1198 [www.emdat.be](http://www.emdat.be) (last access: June 2013), Université Catholique de Louvain, Brussels,  
1199 Belgium, 2013.

1200  
1201 Engelen, G. B. and van Beers, P. H.: Groundwater systems in the eastern Algarve,  
1202 Portugal, in: *Developments in the Analysis of Groundwater Flow Systems*, IAHS Red  
1203 Book Series 163, edited by: Engelen, G. B. and Jones, G. P.,  
1204 UNESCO/IAHS, Wallingford, UK, 325–331, 1986.

1205  
1206 Ferreira, J. G., Simas, T., Nobre, A., Silva, M. C., Shifferegger, K., and Lencart-Silva,  
1207 J.: Identification of Sensitive Areas and Vulnerable Zones in Transitional and Coastal  
1208 Portuguese Systems, Instituto da Água and Institute of Marine Research, 168 pp.,  
1209 available at: <http://www.eutro.org/documents/NEEAPortugal.pdf>, 2003.

1210  
1211 Finkl, C. W. and Krupa, S. L.: Environmental impacts of coastal-plain activities on  
1212 sandy beach systems: hazards, perception and mitigation, *J. Coast. Res.*, SI 35, 132–  
1213 150, 2003.

1214  
1215 Frot, E., van Wesemael, B., Vandenschrick, G., Souchez, R., and Benet, A. S.: Origin  
1216 and type of rainfall for recharge of a karstic aquifer in the western Mediterranean: a  
1217 case study from the Sierra de Gador–Campo de Dalias (southeast Spain), *Hydrol.*  
1218 *Process.*, 21, 359–368, 2007.

1219  
1220 Gat, J. R.: Oxygen and hydrogen isotopes in the hydrologic cycle, *Annu. Rev. Earth*  
1221 *Pl. Sc.*, 24, 225–262, 1996.

1222  
1223 Gat, J. R. and Carmi, I.: Evolution of the isotopic composition of atmospheric waters  
1224 in the Mediterranean Sea area, *J. Geophys. Res.*, 75, 3039–3048, 1970.

1225  
1226 Gat, J. R., Bowser, C. J., and Kendall, C.: The contribution of evaporation from the  
1227 Great Lakes to the continental atmosphere: estimate based on stable isotope data,  
1228 *Geophys. Res. Lett.*, 21, 557–560, 1994.

1229  
1230 Gibson, J. J. and Edwards, T. W. D.: Regional water balance trends and evaporation–  
1231 transpiration partitioning from a stable isotope survey of lakes in northern Canada,  
1232 *Global Biogeochem. Cy.*, 16, 10–11, 2002.

1233  
1234 Gilfedder B.S., Frei S., Hofmann H., and Cartwright I.: Groundwater discharge to  
1235 wetlands driven by storm and flood events: Quantification using continuous Radon-  
1236 222 and electrical conductivity measurements and dynamic mass-balance modeling.  
1237 *Geochimica et Cosmochimica Acta* 165: 161–177, 2015

1238  
1239 Gonnee, M. E., Morris, P. J., Dulaiova, H., and Charette, M. A.: New perspectives  
1240 on radium behavior within a subterranean estuary, *Mar. Chem.*, 109, 250–267, 2008.

1241  
1242 Hampel, F. R.: The influence curve and its role in robust estimation, *J. Am. Stat.*

1243 Assoc., 69, 383–393, 1974.  
1244  
1245 Hancock, G. J. and Murray, A. S.: Source and distribution of dissolved radium in the  
1246 Bega River Estuary, southeastern Australia, *Earth Planet. Sc. Lett.*, 138, 145–155,  
1247 1996.  
1248  
1249 Hancock, G. J., Webster, I. T., Ford, P. W., and Moore, W. S.: Using Ra isotopes to  
1250 examine transport processes controlling benthic fluxes into a shallow estuarine  
1251 lagoon, *Geochim. Cosmochim. Acta*, 64, 3685–3699, 2000.  
1252  
1253 IAEA/WMO: Global Network of Isotopes in Precipitation, The GNIP Database,  
1254 available at: <http://www.iaea.org/water> (last access: June 2014), 2013.  
1255  
1256 Ibánhez, J. S. P., Leote, C., and Rocha, C.: Porewater nitrate profiles in sandy  
1257 sediments hosting submarine groundwater discharge described by an Advection–  
1258 Dispersion-Reaction Model, *Biogeochemistry*, 103, 159–180, 2011.  
1259  
1260 Ibánhez, J. S. P., Leote, C., and Rocha, C.: Seasonal enhancement of Submarine  
1261 Groundwater Discharge (SGD) – derived nitrate loading into the Ria Formosa coastal  
1262 lagoon assessed by 1-D modeling of benthic NO<sub>3</sub>-profiles, *Estuar. Coast. Shelf S.*,  
1263 132, 56–64, 2013.  
1264  
1265 IH – Instituto Hidrografico: Marés 81/82 Ria de Faro. Estudo das marés de oito  
1266 estações da Ria de Faro, Rel. FT-MC 4/86, IH – Instituto Hidrografico, Lisbon, 1986.  
1267  
1268 Kjerfve, B.: Comparative oceanography of coastal lagoons, in: *Estuarine Variability*,  
1269 edited by: Wolfe, D. A., Academic Press, New York, 63–81, 1986.  
1270  
1271 Kroeger, K. D., Swarzenski, P. W., Greenwood, W. J., and Reich, C.: Submarine  
1272 groundwater discharge to Tampa Bay: nutrient fluxes and biogeochemistry of the  
1273 coastal aquifer, *Mar. Chem.*, 104, 85–97, 2007.  
1274  
1275 Kwon, E. Y., Kim, G., Primeau F., Moore W. S., Cho H. M., DeVries T., Sarmiento J.  
1276 L., Charette M. A., and Cho Y. K.: Global estimate of submarine groundwater  
1277 discharge based on an observationally constrained radium isotope model, *Geophysical*  
1278 *Research Letters*, 41(23), 8438-8444, 2014  
1279  
1280 Lee, D. R.: A device for measuring seepage flux in lakes and estuaries, *Limnol.*  
1281 *Oceanogr.*, 22, 140–147, 1977.  
1282  
1283 Leote, C., Ibánhez, J. S., and Rocha, C.: Submarine groundwater discharge as a  
1284 nitrogen source to the Ria Formosa studied with seepage meters, *Biogeochemistry*,  
1285 88, 185–194, 2008.  
1286  
1287 Li, L., Barry, D. A., Stagnitti, F., and Parlange, J.-Y.: Submarine groundwater  
1288 discharge and associated chemical input to a coastal sea, *Water Resour. Res.*, 35,  
1289 3253–3259, 1999.  
1290  
1291 Lobo-Ferreira, J. P., Oliveira, M. M., Diamantino, C., and Leitão, T. E.: LNEC  
1292 Contribution to D24: AR needs in Campina de Faro, Julho, LNEC, Lisbon, 6 pp.,

1293 2007.  
1294  
1295 Macintyre, S., Wanninkhof, R., and Chanton, J. P.: Trace gas exchange across the air-  
1296 sea interface in freshwater and coastal marine environments, in: Biogenic Trace  
1297 Gases: Measuring Emissions from Soil and Water, edited by: Matson, P. A. and  
1298 Harris, R. C., Blackwell Science Ltd, Cambridge, MA, 52–97, 1995.  
1299  
1300 Martin, J. B., Cable, J. E., Swarzenski, P. W., and Lindenberg, M. K.: Enhanced  
1301 submarine ground water discharge from mixing of pore water and estuarine water,  
1302 *Ground Water*, 42, 1000–1010, 2004.  
1303  
1304 Michael H.A., Lubetsky J.S., Harvey C.F.: Characterizing submarine groundwater  
1305 discharge: A seepage meter study in Waquoit Bay, Massachusetts. *Geophysical*  
1306 *research Letters* 30 (6): 1297, 2003  
1307  
1308 Michael, H. A., Mulligan, A. E., and Harvey, C. F.: Seasonal oscillations in water  
1309 exchange between aquifers and the coastal ocean, *Nature*, 436, 1145–1148, 2005.  
1310  
1311 Monteiro, J. P. and Costa Manuel, S.: Dams groundwater modelling and water  
1312 management at the regional scale in a coastal Mediterranean area (the southern  
1313 Portugal Region – Algarve), *Larhyss J.*, 3, 157–169, 2004.  
1314  
1315 Moore, W. S.: Large groundwater inputs to coastal waters revealed by <sup>226</sup>Ra  
1316 enrichments, *Nature*, 380, 612–614, 1996.  
1317  
1318 Moore, W. S.: The subterranean estuary: a reaction zone of ground water and  
1319 seawater, *Mar. Chem.*, 65, 111–125, 1999.  
1320  
1321 Moore, W. S.: Determining coastal mixing rates using radium isotopes, *Cont. Shelf*  
1322 *Res.*, 20, 1993–2007, 2000.  
1323  
1324 Moore, W. S.: The role of submarine groundwater discharge in coastal  
1325 biogeochemistry, *J. Geochem. Explor.*, 88, 389–393, 2006.  
1326  
1327 Moore, W. S.: The effect of submarine groundwater discharge on the ocean, *Annu.*  
1328 *Rev. Mar. Sci.*, 2, 59–88, 2010.  
1329  
1330 Moore, W. S. and Arnold, R.: Measurement of <sup>223</sup>Ra and <sup>224</sup>Ra in coastal waters  
1331 using a delayed coincidence counter, *J. Geophys. Res.-Oceans*, 101, 1321–1329,  
1332 1996.  
1333  
1334 Moore, W. S. and Church, T. M.: Submarine groundwater discharge, *Nature*, 382, p.  
1335 122, 1996.  
1336  
1337 Mudge, S. M., Icely, J. D., and Newton, A.: Residence times in a hypersaline lagoon:  
1338 using salinity as a tracer, *Land Ocean Interactions in the Coastal Zone, LOICZ:*  
1339 *Lessons from Banda Aceh, Atlantis, and Canute, Estuar. Coast. Shelf S.*, 77, 278–284,  
1340 2008.  
1341  
1342 Mulligan, A. E. and Charette, M. A.: Intercomparison of submarine groundwater



1343 discharge estimates from a sandy unconfined aquifer, *J. Hydrol.*, 327, 411–425, 2006.  
1344  
1345 Munksgaard, N. C., Wurster, C. M., Bass, A., Zagorskis, I., and Bird, M. I.: First  
1346 continuous shipboard  $\delta^{18}\text{O}$  and  $\delta\text{D}$  measurements in sea water by diffusion sampling  
1347 – Cavity Ring-Down Spectrometry, *Environ. Chem. Lett.*, 10, 301–307, 2012.  
1348  
1349 Pacheco, A., Ferreira, Ó., Williams, J. J., Garel, E., Vila-Concejo, A., and Dias, J. A.:  
1350 Hydrodynamics and equilibrium of a multiple-inlet system, *Mar. Geol.*, 274, 32–42,  
1351 2010.  
1352  
1353 Prieto, C. and Destouni, G.: Is submarine groundwater discharge predictable?,  
1354 *Geophys. Res. Lett.*, 38, L01402, doi:10.1029/2010GL045621, 2010.  
1355  
1356 Robinson, C., Li, L., and Barry, D. A.: Effect of tidal forcing on a subterranean  
1357 estuary, *Adv. Water Resour.*, 30, 851–865, 2007.  
1358  
1359 Rocha, C., Ibanhez, J., and Leote, C.: Benthic nitrate biogeochemistry affected by  
1360 tidal modulation of Submarine Groundwater Discharge (SGD) through a sandy beach  
1361 face, Ria Formosa, southwestern Iberia, *Mar. Chem.*, 115, 43–58, 2009.  
1362  
1363 Rodgers, P., Soulsby, C., Waldron, S., and Tetzlaff, D.: Using stable isotope tracers to  
1364 assess hydrological flow paths, residence times and landscape influences in a nested  
1365 mesoscale catchment, *Hydrol. Earth Syst. Sci.*, 9, 139–155, doi:10.5194/hess-9-139-  
1366 2005, 2005.  
1367  
1368 Rohling, E. J.: Progress in paleosalinity: overview and presentation of a new  
1369 approach, *Paleoceanography*, 22, PA3215, doi:10.1029/2007PA001437, 2007.  
1370  
1371 Salles, P.: Hydrodynamic Controls on Multiple Tidal Inlet Persistence, PhD thesis,  
1372 Massachusetts Institute of Technology and Woods Hole Oceanographic Institution  
1373 Joint Program in Oceanography/Applied Ocean Sci. and Engineering, Boston, MA,  
1374 2001.  
1375  
1376 Santos, I. R., Burnett, W. C., Chanton, J., Dimova, N., and Peterson, R. N.: Land or  
1377 ocean? Assessing the driving forces of submarine groundwater discharge at a coastal  
1378 site in the Gulf of Mexico, *J. Geophys. Res.*, 114, doi:10.1029/2008JC005038, 2009.  
1379  
1380 Santos, I. R., Eyre, B. D., and Huettel, M.: The driving forces of porewater and  
1381 groundwater flow in permeable coastal sediments: a review, *Estuar. Coast. Shelf S.*,  
1382 98, 1–15, 2012.  
1383  
1384 Schubert, M., Paschke, A., Lieberman, E., and Burnett, W. C.: Air–water partitioning  
1385 of  $^{222}\text{Rn}$  and its dependence on water temperature and salinity, *Environ. Sci.*  
1386 *Technol.*, 46, 3905–3911, 2012.  
1387  
1388 Silva, A. V., Portugal, A., and Freitas, L.: Groundwater flow model and salinization  
1389 of coastal aquifers between Faro and Fuseta, *Comun. Ser. Geol. Portugal*, 72, 71–87,  
1390 1986.  
1391  
1392 Slomp, C. P. and Van Cappellen, P.: Nutrient inputs to the coastal ocean through

1393 submarine groundwater discharge: controls and potential impact, *J. Hydrol.*, 295, 64–  
1394 86, 2004.  
1395  
1396 Spiteri, C., Slomp, C. P., Tuncay, K., and Meile, C.: Modeling biogeochemical  
1397 processes in subterranean estuaries: effect of flow dynamics and redox conditions on  
1398 submarine groundwater discharge of nutrients, *Water Resour. Res.*, 44,  
1399 doi:10.1029/2007WR006071, 2008.  
1400  
1401 Stieglitz, T. C., Cook, P. G., and Burnett, W. C.: Inferring coastal processes from  
1402 regional-scale mapping of <sup>222</sup>Rn and salinity: examples from the Great Barrier  
1403 Reef, Australia, *J. Environ. Radioactiv.*, 101, 544–552, 2010.  
1404  
1405 Stigter, T. Y. and Monteiro, J. P.: Strategies for integrating alternative groundwater  
1406 sources into the water supply system of the Algarve, Portugal, *Water Asset*  
1407 *Management International – IWA 01/2008*, 4, 19–24, 2008.  
1408  
1409 Stigter, T. Y., Carvalho Dill, A. M. M., Ribeiro, L., and Reis, E.: Impact of the shift  
1410 from groundwater to surface water irrigation on aquifer dynamics and hydrochemistry  
1411 in a semi-arid region in the south of Portugal, *Agr. Water Manage.*, 85, 121–132,  
1412 2006.  
1413  
1414 Swarzenski, P. W., Orem, W. H., McPherson, B. F., Baskaran, M., and Wan, Y.:  
1415 Biogeochemical transport in the Loxahatchee River Estuary, Florida: the role of  
1416 submarine groundwater discharge, *Mar. Chem.*, 101, 248–265, 2006.  
1417  
1418 Taniguchi M., Burnett W.C., Smith C.F., Paulsen R.J., O'Rourke D., Krupa S.L.,  
1419 Christoff J.L., Spatial and temporal distributions of Submarine Groundwater  
1420 Discharge rates obtained from various types of seepage meters at a site in the  
1421 Northeastern Gulf of Mexico. *Biogeochemistry* 66, 35-53, 2003.  
1422  
1423 Tett, P., Gilpin, L., Svendsen, H., Erlandsson, C. P., Larsson, U., Kratzer, S.,  
1424 Fouilland, E., Janzen, C., Lee, J.-Y., Grenz, C., Newton, A., Ferreira, J. G.,  
1425 Fernandes, T., and Scory, S.: Eutrophication and some European waters of restricted  
1426 exchange, *Cont. Shelf. Res.*, 23, 1635–1671, 2003.  
1427  
1428 Turner, S. M., Malin, G., Nightingale, P. D., and Liss, P. S.: Seasonal variation of  
1429 dimethyl sulphide in the North Sea and an assessment of fluxes to the atmosphere,  
1430 *Mar. Chem.*, 54, 245–262, 1996.  
1431  
1432 Vila-Concejo, A., Ferreira, Ó., Morris, B. D., Matias, A., and Dias, J. M. A.: Lessons  
1433 from inlet relocation: examples from southern Portugal, *Coast. Eng.*, 51, 967–990,  
1434 2004.  
1435  
1436 Webster, I. T., Hancock, G. J., and Murray, A. S.: Use of radium isotopes to examine  
1437 pore-water exchange in an estuary, *Limnol. Oceanogr.*, 39, 1917–1927, 1994.  
1438  
1439 Webster, I. T., Hancock, G. J., and Murray, A. S.: Modelling the effect of salinity on  
1440 radium desorption from sediments, *Geochim. Cosmochim. Acta*, 59, 2469–2476,  
1441 1995.  
1442

1443 Zektser, I. S. and Loaiciga, H. A.: Groundwater fluxes in the global hydrologic cycle:  
1444 past, present and future, *J. Hydrol.*, 144, 405–427, 1993.  
1445

## 1446 **Figure Captions**

1447

1448 Figure 1. Map showing location of the sampling sites within the Ria Formosa and its  
1449 geographical context. The top panel shows the full geographical extent of the system,  
1450 with the operational separation of the region of interest into western and eastern  
1451 lagoon and the names of all the inlets; The lower panel shows an amplified map of the  
1452 region of interest, including major channels, locations of sampling and tidal stations,  
1453 as well as boundaries of the aquifers bordering the lagoon (M10, M11, M12).

1454 Figure 2. Map showing the distribution of Radon inventories ( $\text{Bq/m}^2$ ) within the main  
1455 channels, during ebb (Panel a) and flood (Panel b), for the radon survey conducted in  
1456 2010. For more details regarding the radon budget in both December 2009 and June  
1457 2010, see Table 1.

1458 Figure 3. Tidal variability of instantaneous radon fluxes, respectively at the inner at  
1459 the Barra Nova inlet (Panel a) and Quatro-Águas station (Panel b), for the radon  
1460 survey conducted in 2010. For more details on calculation methods, please see  
1461 Section 3.1.2.

1462 Figure 4. Catchment isotope hydrology. Anticlockwise, from top left: panel a shows  
1463 the main meteoric water lines framing the isotopic composition of precipitation within  
1464 the catchment, including the precipitation-seawater mixing line (PP-SW Mix, section  
1465 4.2.1.). Panel b plots the isotopic compositional range of water samples taken during  
1466 2007, while Panel c plots the isotopic compositional range of water samples taken  
1467 during the period 2009–2011; the lagoon surface water samples (inset) are shown in  
1468 more detail on Fig. 6. Panel d provides the complete record of daily precipitation over  
1469 the region for the period 2006–2013 for contextual support (see also Table 2 for  
1470 summarized data). EMMWL: Eastern Mediterranean Meteoric Water Line (Gat and  
1471 Carmi 1970); WMMWL: Western Mediterranean Meteoric Water Line (Celle-Jeanton  
1472 et al 2001); GMWL: Global Meteoric Water Line (Clark and Fritz, 1997); LMWL:  
1473 Local Meteoric Water Line (Carreira et al 2005)

1474 Figure 5. Isotopic composition of pore water extracted in winter 2010/2011 (Table  
1475 S1) at different levels depth below the surface at the saturated zone and the dynamics  
1476 of the beach groundwater table. Panel a frames the compositional range and the  
1477 subdivision of the isotopic characteristics through three groups, corresponding to  
1478 different circulation paths within the beach (for explanation, see Section 4.2.3). Panel  
1479 b frames the same samples in a *deuterium excess* ( $d$ ) versus  $\delta^{18}\text{O}$  plot, illustrating the  
1480 progression of evaporative enrichment throughout the three zones and its relationship  
1481 with the LMWL (Local Meteoric Water Line, Carreira et al 2005). Crosses and  
1482 attached error bars represent average compositions for each group. Error bars  
1483 represent  $\pm 1$  s.d.. PP-SW Mix: Precipitation-Seawater Mixing line (section 4.2.1.);  
1484 EMMWL: Eastern Mediterranean Meteoric Water Line (Gat and Carmi 1970);  
1485 WMMWL: Western Mediterranean Meteoric Water Line (Celle-Jeanton et al 2001);  
1486 GMWL: Global Meteoric Water Line (Clark and Fritz, 1997)

1487 Figure 6. Tidal variability of the isotopic composition of surface waters in the  
1488 lagoon, framed by significant local evaporation (LEL), mixing (MX), and meteoric  
1489 lines as well as the average composition of adjacent coastal water and seawater  
1490 (historic data). Panel a: Low tide, and panel b: High tide. For more details, see  
1491 Sections 4.2.4. and 5.2.

1492 Figure 7. Hydrological pathways within the Ria Formosa, as defined by stable  
1493 isotope data. Panel a: 2007 situation — SGD with net input of meteoric water  
1494 present; Panel b: 2009–2011 — SGD essentially derived from tidal pumping.  
1495 Detailed explanations are available in Section 5.3.

1496

1497

1498 **Tables**

1499

1500 **Table 1.** Excess  $^{222}\text{Rn}$  inventories and relevant fluxes supporting the radon mass  
 1501 balance for the Ria Formosa in winter 2009 and summer 2010 (see Sections 4.1  
 1502 and 5.1). Notes: <sup>a</sup>Calculated with formulas 4a and 4b, Section 3.1.4.2; <sup>b</sup>Calculated  
 1503 with Formula 3, Section 3.1.4.1; \*Referenced to lagoon surface area at MTL,  
 1504 calculated using the residual exchange measured at Faro-Olhão adjusted to the  
 1505 residual tidal prisms for all the inlets reported in Pacheco et al. (2010) and cross-  
 1506 section area for all the inlets. Minus sign signifies net export (seaward). \*\*Per  
 1507 unit cross-sectional channel area  
 1508

	Winter 2009	Summer 2010
Tidal Amplitude [m]	2.73	2.51
Wind speed [ $\text{ms}^{-1}$ ]	8.4±8.0	6.3±1.2
<b>Inventories</b>	<b><math>^{222}\text{Rn}</math> inventory ± MAD [<math>\text{Bq m}^{-2}</math>]</b>	
Ebb stage <sup>a</sup>	55.6±30.9	54.2±17.8
Flood stage <sup>a</sup>	73.8±31.5	74.0±17.6
All data <sup>b</sup>	66.1±34.7	65.9±19.6
<b>Fluxes</b>	<b><math>^{222}\text{Rn}</math> flux ± <math>\sigma</math> [<math>\text{Bq m}^{-2} \text{day}^{-1}</math>]</b>	
Diffusion	5.7±1.9	5.9±1.7
Degassing	1.7±1.8	1.1±0.7
Decay	12±6.3	11.9±1.6
Residual Exchange*	-5.26(±1.03)×10 <sup>-4</sup>	-4.74(±0.79)×10 <sup>-4</sup>
<b>Tidal Flux**</b>	<b><math>^{222}\text{Rn}</math> flux ± <math>\sigma</math> [<math>\text{Bq m}^{-2} \text{day}^{-1}</math>]</b>	
<i>Quatro-Águas</i>		
Export	-	85.4±11.1
Import	-	98.6±16.1
Residual	-	13.2±2.8
<i>Barra-Nova</i>		
Export	57.0±6.4	49.8±1.1
Import	65.5±4.2	65.0±4.2
Residual	8.5±1.1	15.2±1.0
<b>Potential Rn sources</b>	<b>Salinity</b>	<b>Activity ± <math>\sigma</math> [<math>\text{Bq m}^{-3}</math>]</b>
Deserta (Well)	0.95	93.8±59.5
Beach porewater	40.6	304±182
Ramalhete (borehole)	5.06	6625±996

1509

1510

1511

1512

1513

1514

1515 **Table 2.** Precipitation records over the region during the sampling campaigns  
 1516 described by this study, as measured at the São Brás de Alportel meteorological  
 1517 station ([www.snirh.pt](http://www.snirh.pt), Ref 31J/C). Monthly precipitation is contrasted with  
 1518 rainfall during the sampling campaigns and compared with historical monthly  
 1519 averages in order to evaluate the relative wetness of the periods in the wider  
 1520 temporal context. Accumulated precipitation during the 3 months prior to the  
 1521 month fieldwork took place is also shown and similarly compared to the  
 1522 historical record average. For a more detailed contextual assessment, the  
 1523 chronological record of daily precipitation for the period 2006-2013 is shown in  
 1524 Fig 4, panel d, with the sampling periods overlain for easy reference when  
 1525 evaluating the stable isotope hydrology of the catchment defined by this study  
 1526 and previous research. Under 'Sampling', and 'Type', the type of endmember  
 1527 collected for stable isotope analysis is shown, except when radon survey  
 1528 campaigns were executed in parallel – in this case 'Radon survey' is added to the  
 1529 column. More details on the individual samples are shown in Table S1.

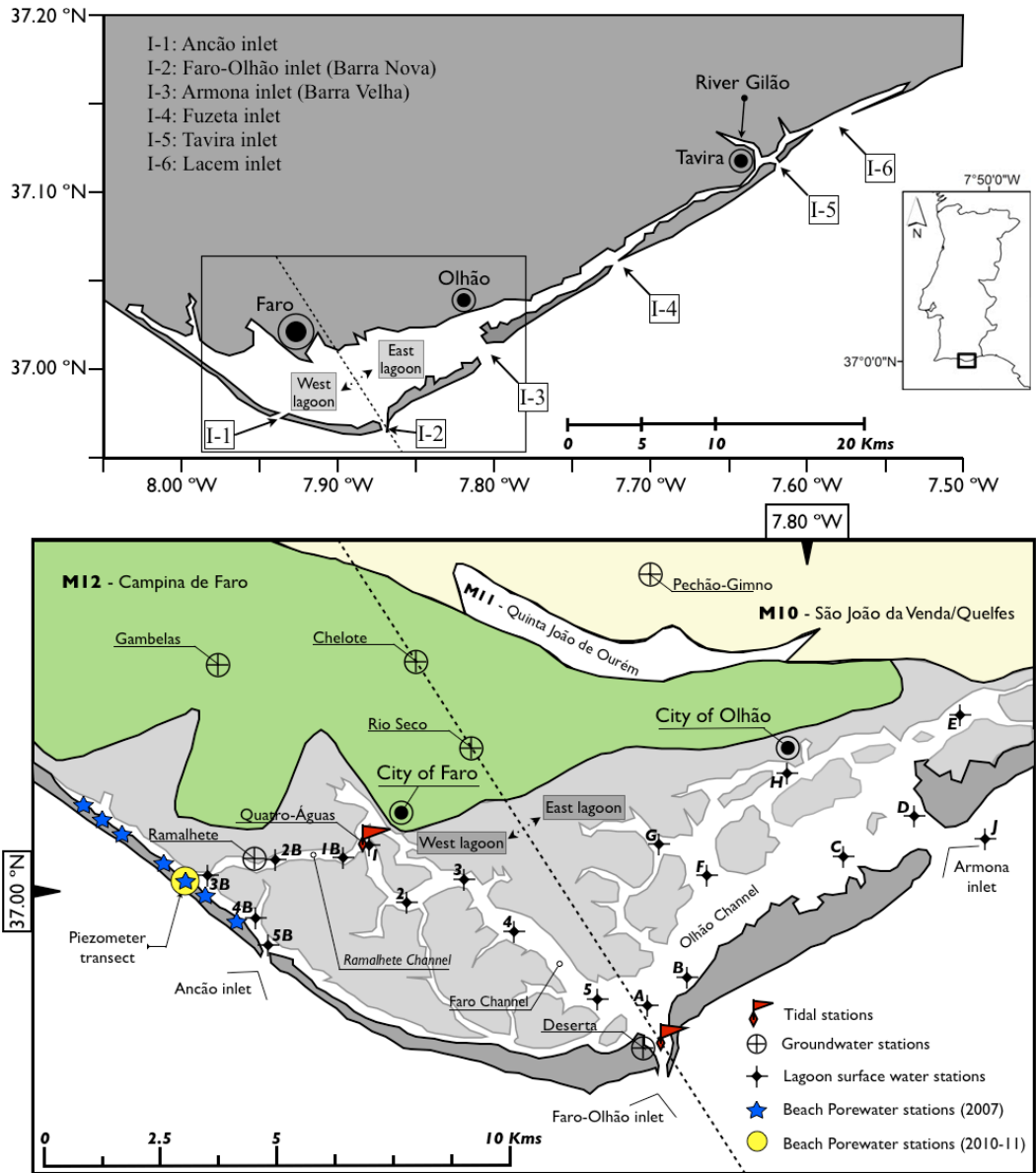
Date	Sampling	Precipitation [mm]					
		Survey	Month		Previous 3 months		
mm/yy	Period	Type	Total	Survey month	Historical average	Total	Historical average
Jan 07	3 <sup>rd</sup> -6 <sup>th</sup>	<u>Groundwater</u> • M12 aquifer • Beach porewater	0.1	8.8	138	369.7	369
July 07	1 <sup>st</sup> -3 <sup>rd</sup>	<u>Groundwater</u> • Beach drainage <u>Surface water</u> • WWTP • Lagoon West	0.0	0.5	3	83.7	125
		<i>Radon survey</i>					
Dec 09	1 <sup>st</sup> -8 <sup>th</sup>	<u>Groundwater</u> • M10 aquifer • M12 aquifer <u>Surface water</u> • Lagoon East • Lagoon West • Seawater <u>Other</u> • Precipitation	10.3	392.2	160	93.6	232
May/June 10	28 <sup>th</sup> -7 <sup>th</sup>	<i>Radon survey</i>	0.0	24.1	16	88.6	207
Dec 10	8 <sup>th</sup> -16 <sup>th</sup>	<u>Groundwater</u> • Beach porewater <u>Surface water</u> • River Gilão	0.5	269.6	160	147	232
Jan 11	3 <sup>rd</sup> -12 <sup>th</sup>	<u>Groundwater</u> • Beach porewater	18.7	48.5	138	414.7	369

1530

1531

1532 New/altered Figures (1&4) – all others remain the same

1533



1534

1535 Figure 1

1536

1537

1538

1539

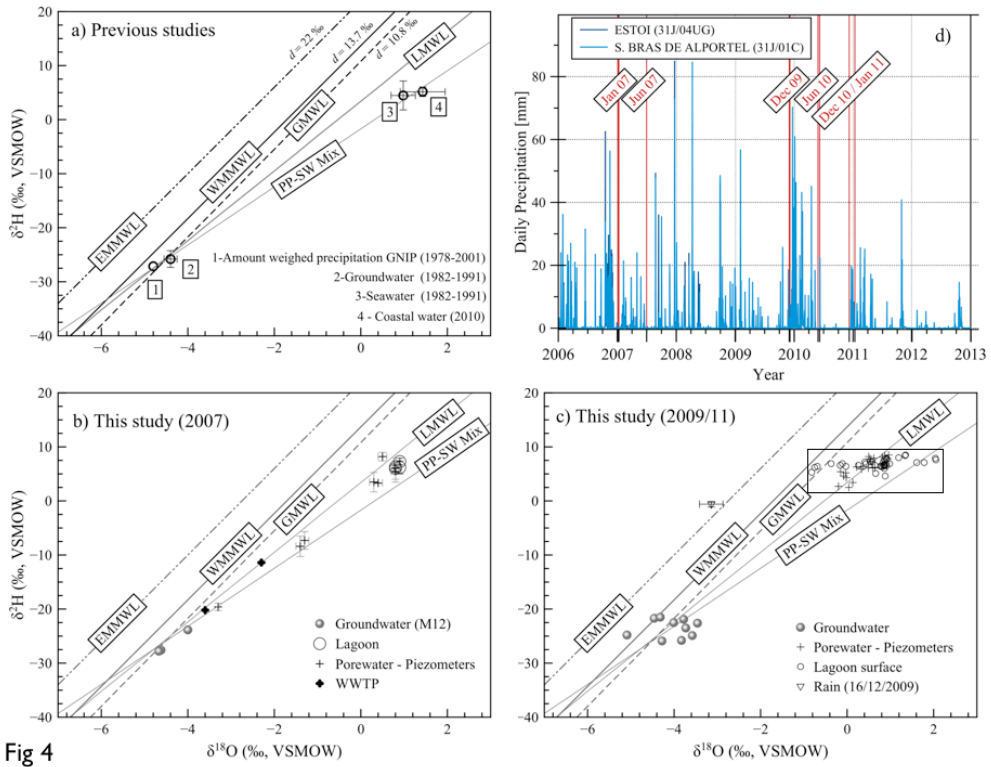


Fig 4

1541

1542

1543 Figure 4

1544

1545

1546

1547

1548